CHALMERS
UNIVERSITY OF TECHNOLOGY

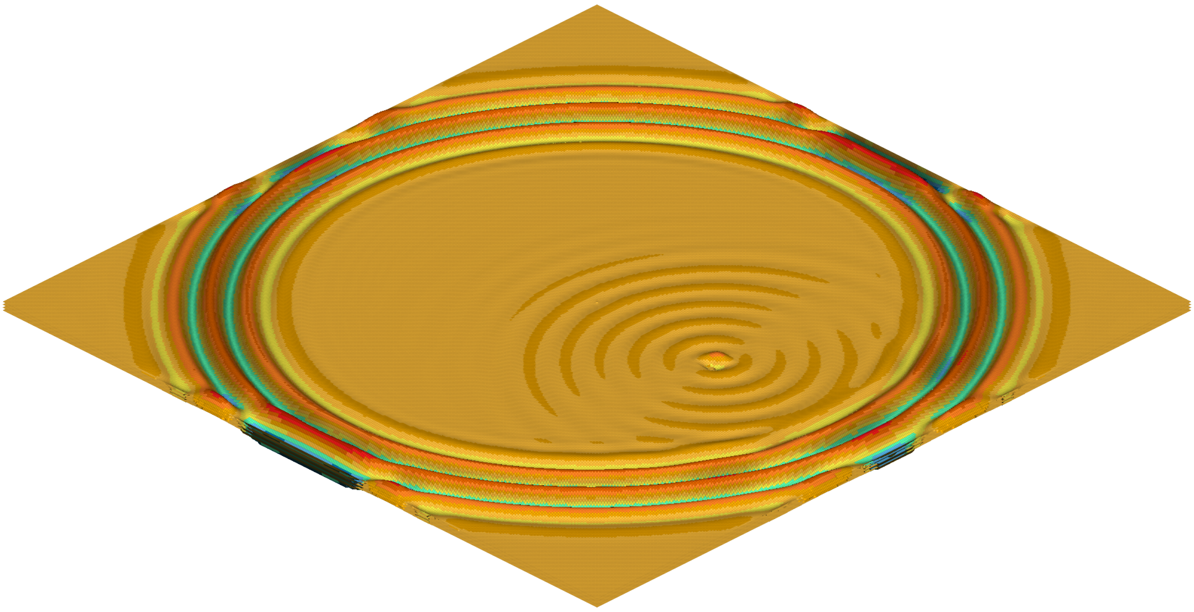

Machine learning for Lamb wave-based delamination detection in composite structures

Master's thesis in Complex Adaptive Systems and Applied Mechanics

GUSTAV GIEBAT & JOEL JANSON

DEPARTMENT OF INDUSTRIAL AND MATERIALS SCIENCE
CHALMERS UNIVERSITY OF TECHNOLOGY
Gothenburg, Sweden 2026
www.chalmers.se

Master's thesis 2026

Machine learning for Lamb wave-based delamination detection in composite structures

GUSTAV GIEBAT
JOEL JANSON

CHALMERS
UNIVERSITY OF TECHNOLOGY

Department of Industrial and Materials Science
Division of Computational Mechanics and Materials Engineering
Chalmers University of Technology
Gothenburg, Sweden 2026

Machine learning for Lamb wave-based delamination detection
in composite structures
GUSTAV GIEBAT, JOEL JANSON

Supervisor: Ruoshan Luo, Saab Surveillance
Examiner: Johanna Xu, Department of Industrial and Materials Science

Master's Thesis 2026
Department of Industrial and Materials Science
Division of Computational Mechanics and Materials Engineering
Chalmers University of Technology
SE-412 96 Gothenburg
Telephone +46 31 772 1000

Cover: Finite element simulation of Lamb wave propagation in a composite plate containing a delamination. The out-of-plane displacement field is shown with a deformation scale factor of 5×10^6.

Typeset in LaTeX
Gothenburg, Sweden 2026

Machine learning for Lamb wave-based delamination detection in composite structures
GUSTAV GIEBAT, JOEL JANSON
Department of Industrial and Materials Science
Chalmers University of Technology

Abstract

Composite materials are increasingly used in the aerospace industry due to their high strength-to-weight ratio and favourable mechanical properties. However, composite structures are susceptible to complex failure mechanisms such as delamination, while conventional inspection and maintenance procedures are often expensive and time consuming. Structural health monitoring based on guided Lamb waves has therefore emerged as a promising approach for automated damage detection. This thesis investigates a methodology for delamination detection and localisation in composite plates by combining finite element simulations of guided Lamb waves with machine learning. Finite element simulations were performed to model wave propagation in undamaged and delaminated plates, generating a dataset used to train and evaluate a one-dimensional convolutional neural network (CNN). Three plate sizes were considered, and the influence of noise level and training dataset size was examined. For delamination detection, the proposed CNN achieved classification accuracies of $(96.4\% \pm 7.0\%)$, $(99.4\% \pm 0.5\%)$, and $(78.0\% \pm 23.0\%)$ on the 100 mm, 250 mm, and 500 mm plates, respectively, at a signal-to-noise ratio of 20 dB. For localisation, the corresponding mean squared errors were (0.00191 ± 0.00092), (0.00232 ± 0.00043), and (0.01068 ± 0.00240). The results demonstrate that finite element simulations can be used to generate datasets suitable for machine learning-based structural health monitoring, and that the proposed CNN can accurately detect and localise delaminations under favourable noise and training data conditions.

Keywords: Lamb Waves, Structural Health Monitoring, Composites, Delamination, Damage Detection, Damage Localisation, Machine Learning, Convolutional Neural Networks, Finite Element Method.

Acknowledgements

We would like to express our sincere gratitude to Saab for providing us with the opportunity to carry out this exciting thesis project and for creating an inspiring and supportive working environment.

We are especially grateful to Ruoshan Luo, our industrial supervisor, for valuable guidance, technical expertise, and continuous support throughout the project. Her insights and feedback have been invaluable in shaping the direction of this work.

We would also like to thank Johanna Xu, examiner at Chalmers University of Technology, for ensuring the academic quality of the thesis throughout the examination process.

Finally, we would like to thank our colleagues at Saab and Aria Ravantab at Ansys for their willingness to share knowledge and provide technical assistance, helping us resolve simulation-related challenges encountered during the project.

Gustav Giebat & Joel Janson
Gothenburg, June 2026

List of Acronyms

Below is the list of acronyms that have been used throughout this thesis listed in alphabetical order:

ANN	Artificial Neural Network
CFL	Courant-Friedrichs-Lewy
CFRP	Carbon Fibre Reinforced Polymer
CNN	Convolutional Neural Network
FEM	Finite Element Method
MSE	Mean Squared Error
ReLU	Rectified Linear Unit
RMSE	Root Mean Squared Error
SGD	Stochastic Gradient Descent
SHM	Structural Health Monitoring
SNR	Signal-to-Noise Ratio

Contents

List of Figures

List of Tables

1

Introduction

1.1 Background

The increasing use of composite materials in the aerospace industry has created a growing demand for reliable methods to ensure long-term structural integrity. Due to their high specific strength and stiffness, composite structures enable significant weight reductions compared to conventional metallic materials, thereby improving fuel efficiency and overall performance. However, the complex failure mechanisms of composites, particularly internal damage such as delamination, present major challenges for inspection and maintenance. As aerospace structures are subjected to fatigue, impact events, and operational loading throughout their service life, structural degradation is unavoidable. Traditional maintenance strategies often rely on scheduled inspections, which may be costly, time-consuming, and inefficient. Structural health monitoring (SHM) has therefore emerged as an increasingly important field, aiming to continuously assess structural integrity, detect damage at an early stage, and utilise predictive maintenance [1].

A common approach in SHM is to use actuators and sensors to excite and measure vibrations in a structure, and then infer its condition from the resulting wave data. Lamb waves, which are guided ultrasonic waves that propagate in thin-walled components, are widely employed for monitoring composite materials. The ability to propagate over relatively large distances while remaining sensitive to internal defects makes Lamb waves suitable for SHM applications. Their use, however, is complicated by the nature of wave propagation in anisotropic media, which typically involves strong dispersion, multiple coexisting modes, and complex boundary reflections [2].

To better understand and exploit guided wave behaviour, finite element modelling has become an essential tool for simulating Lamb wave propagation and wave–damage interactions under controlled conditions. Numerical simulations offer the possibility to systematically investigate different damage scenarios while avoiding the cost and practical limitations associated with large-scale experimental testing. An additional advantage is the ability to efficiently generate large quantities of labelled data, where the damage state and location are known a priori. Such datasets are particularly valuable for supervised machine learning, which typically requires extensive training data to learn complex relationships between measured signals and structural condition.

Among machine learning approaches, both one-dimensional and two-dimensional convolutional neural networks (CNNs) have demonstrated strong performance for pattern recognition in time-series data. By automatically extracting relevant features directly from either raw sensor signals or frequency spectrograms, CNNs can identify subtle changes in waveforms associated with structural damage. Consequently, CNN-based methods have received increasing attention within structural health monitoring for tasks such as damage detection, classification, and localisation [3], [4], [5].

A master's thesis conducted in 2025 by Lundgren and Lindström [6] developed a finite element-based methodology for simulating Lamb wave propagation in composite plates. Simulations were carried out using LS-DYNA, which is an explicit finite element solver. Their work demonstrated that guided wave simulations could successfully detect and localise damage such as cracks and delaminations by analysing changes in wave amplitude and arrival time. While the previous work successfully demonstrated numerical damage detection capabilities, the interpretation of wave signals remained largely analysis-driven. The increasing availability of machine learning techniques presents an opportunity to automate damage detection and localisation by learning directly from simulated wave responses.

The present thesis builds upon the modelling methodology developed by Lundgren and Lindström [6] by extending it with large-scale dataset generation and supervised machine learning. In particular, CNNs are investigated for automated detection and localisation of delamination in composite plates using simulated Lamb wave data. By combining finite element simulations with data-driven learning, the work contributes towards the development of automated SHM systems for composite structures.

1.2 Aim

The aim of this thesis is to develop a methodology for delamination detection and localisation in composite structures through the combined use of finite element simulations and machine learning. To achieve this, the work is divided into two main parts:

1. Employ a finite element model to simulate guided wave propagation in both undamaged and delaminated composite structures, thereby generating structured datasets for machine learning applications.

2. Design, train, and evaluate an artificial neural network with the purpose of performing delamination detection and localisation based on the simulated sensor data.

1.3 Research questions

In accordance with the aim of this thesis, the following research questions are addressed:

1. How can finite element simulations of Lamb wave propagation in composite laminates be used to generate datasets suitable for machine learning?
2. How can machine learning models be trained to detect and localise delamination in composite structures using guided wave data?
3. How does a convolutional neural network compare to benchmark models in terms of detection and localisation performance under various conditions?

1.4 Scope and limitations

To ensure the completion of the project within the available timeframe, several limitations are defined.

The geometrical complexity of the investigated structure is restricted to square composite plates of three different sizes. The study is therefore limited to a simplified structural representation and does not include more complex aerospace geometries or structural features. Only delamination is considered as the damage mechanism in this work. Other common composite damage modes, such as matrix cracking, fibre breakage, or impact-induced damage, are excluded. Furthermore, the thesis focuses solely on damage detection and localisation, and does not investigate the physical mechanisms governing damage initiation or progression.

Wave excitation from piezoelectric transducers is idealised through prescribed nodal displacements rather than fully coupled electromechanical transducer modelling. While this approach enables efficient simulation of guided wave propagation, it does not capture the complete physical behaviour of real actuator systems.

All datasets used for machine learning are generated through numerical simulations, meaning that no experimental validation is performed within the scope of this work. Consequently, potential discrepancies between simulated and real-world sensor data are not addressed.

Finally, environmental influences such as temperature variations, humidity, material ageing, and operational uncertainties are neglected. The material properties are therefore assumed to remain constant throughout all simulations.

1.5 Thesis outline

This thesis is structured into six main chapters, each addressing a specific part of the research process.

- **Chapter 1: Introduction**
  Establishes the background and motivation for structural health monitoring of composite structures. Defines the research questions and outlines the scope and limitations of the present work.
- **Chapter 2: Theory**
  Presents the theoretical framework necessary for the thesis, including compos-

ite materials, damage mechanisms, guided wave propagation, finite element modelling criteria, and relevant machine learning concepts.

- **Chapter 3: Methodology**
  Describes the numerical modelling methodology, simulation setup, dataset generation process, and machine learning implementation used to detect and localise delamination in composite structures.
- **Chapter 4: Results**
  Presents the results obtained from the finite element simulations and the machine learning models, evaluating the performance of delamination detection and localisation.
- **Chapter 5: Discussion**
  Interprets and discusses the obtained results in relation to the adopted methodology and the limitations of the study.
- **Chapter 6: Conclusion**
  Summarises the main outcomes of the thesis, answers the research questions, and provides recommendations for future work.

2

Theory

This chapter presents the theoretical background necessary for understanding the present work. It includes fundamental concepts related to composite materials, Lamb wave propagation, finite element modelling criteria for guided wave simulations, and the machine learning methods used for delamination detection and localisation.

2.1 Composites

Composite materials have become increasingly important in the aerospace industry due to their high specific strength, high specific stiffness, and superior fatigue and corrosion resistance compared to conventional metallic materials. These properties enable substantial structural weight reduction while maintaining mechanical performance, which is essential for improving fuel efficiency and payload capacity in aerospace applications [7].

A composite material is generally defined as a combination of two or more distinct constituent materials that together produce mechanical properties superior to those of the individual components alone. In fibre-reinforced polymer composites, these constituents primarily consist of reinforcing fibres embedded within a surrounding matrix material. The fibres provide the primary load-carrying capability and stiffness, while the matrix binds the fibres together, transfers loads between them, and protects them from environmental and mechanical damage [7].

Carbon fibre reinforced polymers (CFRPs) are anisotropic, with stiffness and strength strongly dependent on fibre orientation. One single fibre reinforced layer of such a composite is called a ply, or lamina, and by stacking multiple plies with different fibre orientations, a laminate is formed. The stacking sequence of the plies governs the overall structural response and allows engineers to tailor the mechanical properties of the laminate for specific loading conditions. Symmetric and quasi-isotropic layups are commonly used in aerospace structures to achieve balanced mechanical behaviour while minimising undesirable coupling effects [7].

2.1.1 Damage modes

Despite their favourable structural properties, composite materials are susceptible to several damage mechanisms that differ from those typically observed in isotropic metallic structures. Common damage modes include matrix cracking, fibre breakage, fibre-matrix debonding, and delamination.

Among these, delamination is one of the most critical forms of damage in laminated composites. Delamination refers to the separation of adjacent plies due to failure within the interlaminar region. An illustrated example can be seen in Figure 2.1. Delamination can be caused by impact loading, fatigue, manufacturing defects, or interlaminar stress concentrations. Because this damage often occurs beneath the laminate surface, it can be difficult to detect through visual inspection alone while still significantly reducing structural stiffness, strength, and load transfer capability [7].

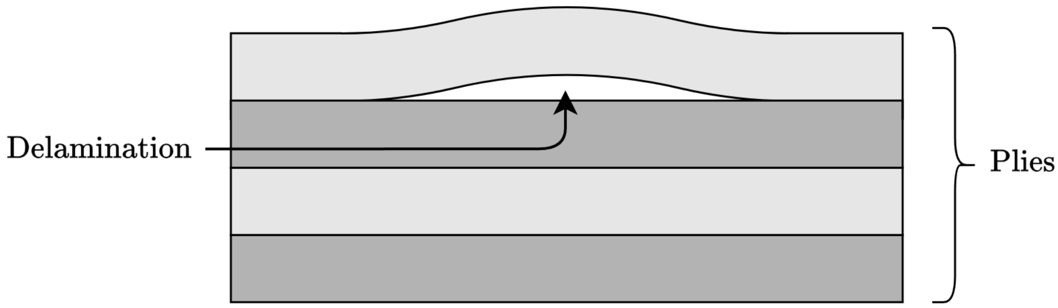

Figure 2.1: Illustration of interlaminar delamination between two plies.

From the perspective of guided wave propagation, delamination introduces local discontinuities that can alter wave behaviour through scattering, reflection, and mode conversion [2]. These effects make delamination particularly suitable for structural health monitoring using Lamb waves. Since delamination represents both a critical structural threat and a detectable wave-interaction mechanism, it is selected as the sole damage mode considered in the present work.

2.2 Lamb waves

Lamb waves are a class of guided elastic waves that propagate in solid plates bounded by two parallel free surfaces. The particle motion lies within the plane defined by the direction of wave propagation and the direction perpendicular to the plate. Unlike bulk waves, which travel through an infinite medium, Lamb waves are constrained by the plate geometry, causing repeated reflections between the upper and lower surfaces. This confinement produces complex wave behaviour characterised by multiple propagation modes and strong dispersion. As a result, the propagation velocity of Lamb waves depends on both frequency (f) and plate thickness (d), commonly expressed through the frequency-thickness product, fd [8].

There are several characteristics that make Lamb waves highly attractive for structural health monitoring applications. At higher excitation frequencies, Lamb waves exhibit relatively short wavelengths, which improves their sensitivity to small internal defects such as cracks, delaminations, and material degradation. Additionally, Lamb waves experience relatively low geometrical attenuation, with amplitude decay proportional to $1/\sqrt{r}$, where r is the propagation distance from the source [9]. This allows them to propagate over long distances while retaining sufficient signal strength for reliable monitoring. These properties make Lamb waves suitable for damage detection in thin-walled composite structures.

In laminated CFRP structures, however, Lamb wave propagation is strongly influenced by material anisotropy. Since the stiffness of the laminate varies with fibre orientation, both the wave velocity and attenuation become direction-dependent. As a result, waves propagating along different directions may arrive at different times and with different amplitudes, even when travelling the same distance. Furthermore, anisotropy can distort the wavefront from the circular shape typically observed in isotropic plates, leading to more complex propagation patterns. These characteristics must be considered when interpreting measured signals and designing structural health monitoring systems for composite structures [8], [10].

2.2.1 Wave modes

Lamb waves exist in two primary mode families: symmetric modes, denoted by S_n, and antisymmetric modes, denoted by A_n, where $n \in \mathbb{N} \cup \{0\}$ represents the mode order. Symmetric modes involve particle motion that is symmetric about the plate mid-plane, while antisymmetric modes exhibit out-of-plane motion that is antisymmetric about the mid-plane [10]. An illustration of symmetric and antisymmetric modes can be seen in Figure 2.2.

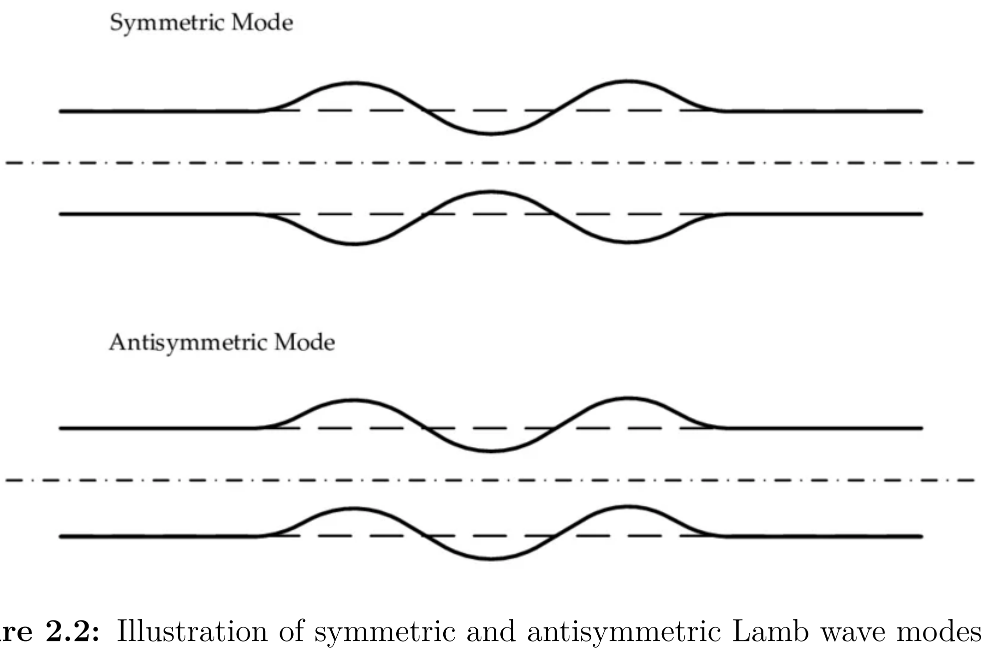

Figure 2.2: Illustration of symmetric and antisymmetric Lamb wave modes [11].

For a given frequency-thickness product, multiple Lamb wave modes may coexist. As the value of fd increases, additional higher-order modes become excitable. At low frequency-thickness products, however, only the two fundamental modes are present: the fundamental symmetric mode (S_0) and the fundamental antisymmetric mode (A_0) [8].

The S_0 mode generally exhibits higher propagation velocity and is primarily associated with extensional deformation, where particle motion is dominated by in-plane stretching of the plate. In contrast, the A_0 mode is typically characterised by flexural behaviour, involving more pronounced out-of-plane bending motion and lower propagation velocity. Due to its increased sensitivity to thickness variations, local stiffness reductions, and interlaminar defects, the A_0 mode is particularly well-suited for delamination detection in composite laminates [2], [8], [12].

In the present work, excitation is specifically designed to selectively generate the fundamental A_0 mode, as this mode provides favourable damage sensitivity while limiting the complexity associated with multimodal wave propagation.

2.3 FE modelling criteria for wave propagation

Finite element simulations of guided wave propagation require careful numerical discretisation in both space and time to ensure accurate representation of the wave behaviour. Due to the high frequencies and short wavelengths involved, insufficient mesh density or inappropriate time step selection may lead to numerical dispersion, instability, or excessive computational cost.

2.3.1 Mesh criteria

For wave propagation problems, the spatial discretisation must be sufficiently fine to accurately capture the wavelength of the propagating mode. A commonly accepted criterion is that at least ten elements per wavelength should be used to minimise numerical dispersion and ensure accurate prediction of wave speed and signal characteristics [13]. Numerical dispersion refers to artificial changes in wave velocity introduced by the numerical discretisation.

The wavelength, λ, is related to the phase velocity, c_p, and excitation frequency, f, according to

$$\lambda = \frac{c_p}{f}. \tag{2.1}$$

Based on this, the maximum allowable element size, h, can be expressed as

$$h \leq \frac{\lambda}{N}, \tag{2.2}$$

where N is the desired number of elements per wavelength, typically chosen as $N \geq 10$.

2.3.2 Time step criteria

In explicit finite element simulations, the stable time increment is governed by the Courant-Friedrichs-Lewy (CFL) stability condition. To maintain numerical stability, the time step must be sufficiently small such that the propagating wave does not travel through more than a fraction of an element during a single increment.

The stability criterion can be expressed as

$$\Delta t \leq \frac{h}{c_p} C_{\max}, \tag{2.3}$$

where Δt is the time step, c_p is the phase velocity, and $C_{\max}$ is the maximum allowable Courant number. The Courant number is typically chosen between $0.5 < C_{\max} < 1$ for explicit applications and can be considered as a safety factor [14].

This criterion implies that decreasing the element size to improve spatial accuracy also reduces the allowable time step, thereby increasing computational cost. As a result, time step and mesh size are strongly coupled, and a balance between spatial resolution and temporal stability is required while maintaining reasonable computational demands.

In LS-DYNA, the stable time step for square shell elements is estimated as

$$\Delta t_{\mathrm{LS}} = t_{\mathrm{SF}} \cdot \frac{h}{c}, \tag{2.4}$$

where h is the characteristic element length, t_{SF} is a time step scale factor (typically 0.9), and c is the effective wave speed used by LS-DYNA to estimate the critical time step. Unlike the phase velocity c_p in (2.3), which describes the propagation speed of the selected Lamb wave mode, c represents a material-dependent elastic wave speed that governs numerical stability. Consequently, the time step calculated by LS-DYNA is generally conservative with respect to the CFL criterion for the propagating Lamb wave. The effective wave speed may be approximated by

$$c = \sqrt{\frac{E}{\rho(1-\nu^2)}}, \tag{2.5}$$

where E is Young's modulus, ρ is the material density, and ν is Poisson's ratio.

For composite materials, the critical time step is evaluated individually for each element based on its effective local stiffness properties. Consequently, no single global value of E or ν governs the time step for the entire model [15].

2.4 Machine learning

Machine learning methods aim to identify patterns and relationships in data in order to make predictions on previously unseen samples. Such methods can broadly be divided into traditional machine learning algorithms and artificial neural networks (ANNs).

This section introduces one ANN-based method, CNNs, as well as two traditional machine learning algorithms: ridge regression and logistic regression.

2.4.1 Convolutional neural networks

CNNs were originally introduced for object recognition and image classification, but have since been extended to other forms of structured data, including one-dimensional time series [16]. The main focus will be on one-dimensional CNNs, since they are of primary relevance to this thesis. Nevertheless, all concepts and methods presented can be generalised to CNNs in two or more dimensions.

A CNN typically consists of convolutional layers, activation functions, pooling layers, and fully connected layers. Each convolutional layer consists of a number of feature maps (also referred to as channels). A feature map is obtained by convolution of the input signal with a learnable filter, also referred to as a kernel [17]. For a one-dimensional input signal x, the discrete convolution operation with a kernel of size k can be expressed as

$$\sum_{j=1}^{k} x_{i+j} w_j - \theta, \tag{2.6}$$

where w_j is weight j of the kernel and θ is the threshold. Following the convolutional operation a non-linear activation function is applied, resulting in

$$y_i = g\left(\sum_{j=1}^{k} x_{i+j} w_j - \theta\right), \tag{2.7}$$

where $g(\cdot)$ is the non-linear activation function and y_i denotes the feature map value at position i. One of the most widely used activation functions is the rectified linear unit (ReLU), defined as

$$g(x) = \max(0, x). \tag{2.8}$$

Multiple convolutional filters are typically employed in each layer, allowing the network to learn different types of signal features [17].

Pooling layers are often introduced between convolutional layers to reduce the dimensionality of the feature maps and thereby decreasing computational cost and increasing regularisation. One common method is max-pooling, where the maximum value within a window is retained [17].

The final part of a CNN typically consists of one or more fully connected layers, which use the extracted features to perform classification or regression tasks.

In supervised learning, both the weights of the fully connected layers and the convolutional kernels are updated iteratively in order to minimise a loss function. The choice of loss function depends on the specific task and optimisation objective. Common optimisation algorithms used for training neural networks include stochastic gradient descent (SGD) and the Adam optimiser [16].

2.4.2 Ridge regression

Consider the linear regression problem

$$Y = X\beta + \epsilon, \tag{2.9}$$

where $X \in \mathbb{R}^{n \times p}$ is the design matrix, $\beta \in \mathbb{R}^{p \times 1}$ is the parameter vector, and ϵ represents normally distributed noise. A common approach for estimating the model parameters β is the method of least squares. The corresponding parameter estimate is given by

$$\hat{\beta} = (X^\intercal X)^{-1} X^\intercal Y, \tag{2.10}$$

where $\hat{\beta}$ denotes the least-squares estimate of the parameter vector.

To perform the parameter estimation in (2.10), the matrix $X^\intercal X$ must be invertible. This condition may fail, or the matrix may become ill-conditioned, when the number of features, p, exceeds the number of samples, n, i.e. when $p > n$. To obtain a parameter estimate in such cases, a positive regularisation parameter α can be added to the diagonal of $X^\intercal X$, as proposed by Arthur E. Hoerl [18]. This approach is known as ridge regression, for which the parameter estimate is given by

$$\hat{\beta}^* = (X^\intercal X + \alpha I)^{-1} X^\intercal Y. \tag{2.11}$$

2.4.3 Logistic regression

Logistic regression is a supervised machine learning method commonly used for binary classification problems. In contrast to linear regression, which predicts continuous values, logistic regression models the probability that a sample belongs to a particular class [19].

Given an input vector $x \in \mathbb{R}^p$, logistic regression models the probability of belonging to the positive class as

$$P(y = 1 \mid x) = \sigma(z), \tag{2.12}$$

where

$$z = \beta^\intercal x + b, \tag{2.13}$$

and where β denotes the parameter vector, b is a bias term, and $\sigma(\cdot)$ is the sigmoid activation function defined as

$$\sigma(z) = \frac{1}{1 + e^{-z}}. \tag{2.14}$$

The sigmoid function maps the linear output z to the interval $(0, 1)$, allowing the output to be interpreted as a probability.

Model parameters are estimated by maximising the likelihood. For logistic regression, this is equivalent to minimising the binary cross-entropy loss function,

$$L(y, \hat{\mu}) = -\left[y \log(\hat{\mu}) + (1 - y) \log(1 - \hat{\mu}) \right], \tag{2.15}$$

where $y \in \{0, 1\}$ denotes the true class label and $\hat{\mu}$ represents the predicted probability [19].

To reduce overfitting and improve numerical stability, logistic regression commonly employs regularisation. In the case of L_2-regularisation, the optimisation problem becomes

$$\min_{\beta} \left[\sum_{i=1}^{n} L(y_i, \hat{y}_i) + \lambda \beta^\intercal \beta \right], \tag{2.16}$$

where λ is the regularisation parameter [19].

3

Methodology

This chapter presents the methodology employed in the present work. It includes the development and configuration of the finite element simulations used for guided wave data generation, as well as the design and implementation of the machine learning framework for delamination detection and localisation.

3.1 Finite element modelling

The numerical modelling methodology used in this work was primarily based on the master's thesis by Lundgren and Lindström [6], in which guided wave propagation in composite structures was investigated using explicit finite element simulations. In the present study, the approach was adapted and extended to enable the generation of extensive datasets of delamination scenarios intended for machine learning-based SHM.

All simulations were performed using the explicit finite element solver LS-DYNA (MPP R16.1.1), with pre-processing carried out in ANSA (v25.2.0). The objective was to simulate Lamb wave propagation in a composite laminate, both in undamaged and delaminated configurations.

3.1.1 Geometry and structural discretisation

The model geometry consisted of a square composite plate with side length L and a total thickness of 4 mm. The geometry and coordinate system are illustrated in Figure 3.1. Three plate sizes were considered, with side lengths of 100 mm, 250 mm, and 500 mm.

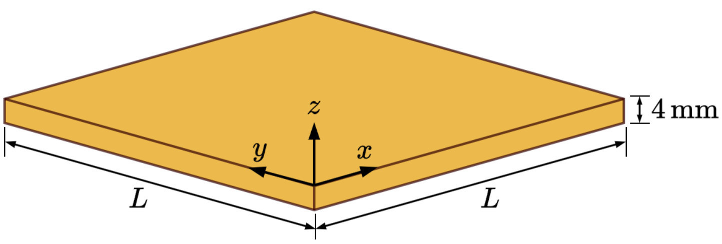

Figure 3.1: Illustration of the plate geometry and coordinate system. Three plate sizes were considered, with $L = 100$ mm, 250 mm, and 500 mm.

A global Cartesian coordinate system was defined with its origin located at the plate corner shown in Figure 3.1. The x- and y-axes correspond to the in-plane directions of the plate, while the z-axis corresponds to the out-of-plane direction.

The stacking sequence of the composite laminate was defined as

$$[0/90/45/-45]_{S4}, \tag{3.1}$$

where the numbers denote the fibre orientation angle (in degrees) of each ply relative to the global x-axis. The subscript $S4$ indicates that the layup is first mirrored about the laminate midplane to form a symmetric 8-ply sublaminate, which is subsequently repeated four times, yielding a total of 32 plies. An illustration of the stacking sequence is shown in Figure 3.2. The material coordinate system is defined locally for each ply, with material axis 1 aligned with the fibre direction. Consequently, the material axes are not fixed globally but rotate according to the fibre orientation of each ply.

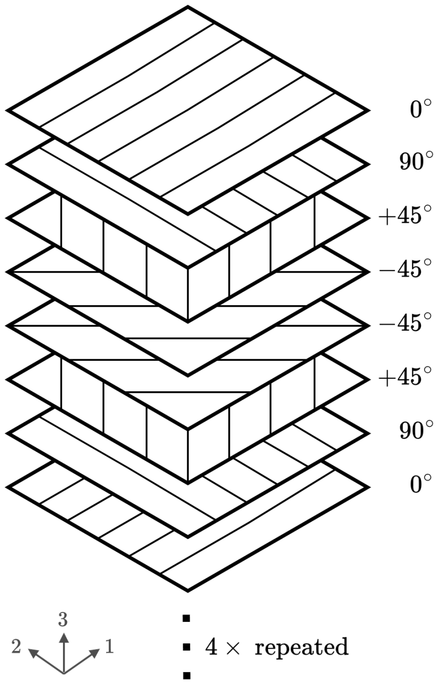

Figure 3.2: Illustration of stacking sequence $[0/90/45/-45]_{S4}$.

Several modelling strategies exist for representing laminated composite structures in finite element simulations. A fully resolved approach involves modelling each individual ply as a separate shell layer, resulting in 32 distinct layers. While this provides high through-thickness resolution, it leads to a substantial increase in computational cost, particularly for explicit simulations where the stable time step is governed by the smallest element dimension.

Alternatively, the laminate may be modelled using solid elements. Although this approach enables a continuous through-thickness representation, it requires a very fine mesh in the thickness direction to accurately capture high-frequency wave propagation, which again results in a high computational cost.

In the present work, a compromise between accuracy and computational efficiency was adopted. The laminate was discretised into four shell layers, each with stacking sequence $[0/90/45/-45]_S$, corresponding to eight plies per shell. Within each shell layer, the individual ply orientations and material properties were retained through the laminate definition, allowing the stiffness of each eight-ply sublaminate to be computed from the constituent ply properties. Consequently, the overall mass distribution, anisotropic behaviour, and laminate stiffness were preserved while significantly reducing the number of elements and associated computational cost. However, the adopted discretisation represents an approximation of the physical laminate, since detailed through-thickness stress, strain, and displacement variations within each eight-ply shell cannot be resolved explicitly.

Fully integrated shell elements were employed to improve the accuracy of bending-dominated behaviour and wave propagation while avoiding spurious zero-energy deformation modes (hourglass modes) that may occur in formulations with reduced integration [15]. A visualisation of the adopted shell-based representation is shown in Figure 3.3a, while a visualisation of the full 32-ply laminate is shown in Figure 3.3b.

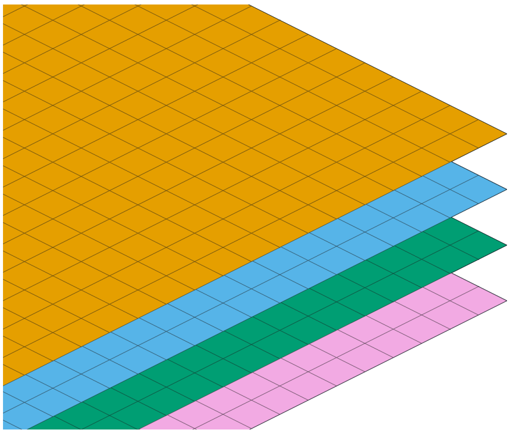

(a) Shell representation.

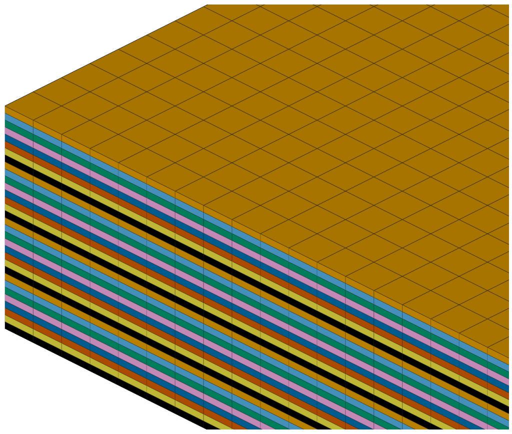

(b) Ply-level representation.

Figure 3.3: Visualisation of the laminate discretisation in ANSA. The four shells in (a) each contain eight plies, resulting in the 32-ply laminate shown in (b).

An additional advantage of the adopted discretisation strategy was that it enabled explicit modelling of interlaminar behaviour through contact definitions between adjacent shell layers. This facilitated the introduction of delamination by locally modifying the interfacial constraints, which would not have been feasible in a single-layer shell model. Compared with a fully ply-resolved representation, delaminations could only be introduced at the interfaces between the four shell layers rather than between arbitrary plies. A more detailed description of the delamination modelling approach is provided in Section 3.1.3.

3.1.2 Material modelling

Each ply of the composite was modelled as a linear elastic orthotropic material. The material represented a unidirectional T700S CFRP lamina. As illustrated in Figure 3.2, material axis 1 was aligned with the fibre direction, while axes 2 and 3 corresponded to the transverse directions. The material properties were defined in accordance with classical lamination theory conventions and are listed in Table 3.1.

Table 3.1: Material properties of the unidirectional T700S CFRP lamina. Material axis 1 is aligned with the fibres, while axes 2 and 3 are transverse to the fibres.

Property	Value	Unit	Description
ρ	1800	kg/m^3	Mass density
E_1	139	GPa	Young's modulus in fibre direction (1)
E_2	8.5	GPa	Young's modulus in transverse direction (2)
E_3	8.5	GPa	Young's modulus in transverse direction (3)
G_{12}	4.2	GPa	In-plane shear modulus (1–2 plane)
G_{13}	4.2	GPa	Shear modulus (1–3 plane)
G_{23}	2.2	GPa	Transverse shear modulus (2–3 plane)
ν_{12}	0.24	–	Poisson's ratio (1–2)
ν_{13}	0.24	–	Poisson's ratio (1–3)
ν_{23}	0.40	–	Poisson's ratio (2–3)

The remaining Poisson's ratios were calculated such that the reciprocity conditions for an orthotropic material were satisfied. These relations are given by

$$\nu_{21} = \nu_{12}\frac{E_2}{E_1}, \quad \nu_{31} = \nu_{13}\frac{E_3}{E_1}, \quad \nu_{32} = \nu_{23}\frac{E_3}{E_2}. \tag{3.2}$$

3.1.3 Contact and delamination modelling

The interaction between adjacent shell layers was modelled using a tied contact formulation with an offset between the connected surfaces. This approach constrains the relative motion between neighbouring layers while accounting for the physical distance between their mid-surfaces. From a numerical standpoint, the formulation enforces displacement compatibility by coupling the translational degrees of freedom of one surface to the interpolated motion of the opposing surface. The offset is incorporated directly into the constraint equations, allowing the kinematics of the layered structure to be represented without requiring coincident nodes. This is particularly important for shell-based laminate models, as it avoids artificial stiffening and provides a more realistic representation of bending behaviour [15].

Delamination was introduced by locally removing the contact condition between two adjacent shell layers. This resulted in a complete loss of displacement constraint within the specified region, allowing the neighbouring layers to move and separate independently of one another. Physically, this corresponds to an interlaminar crack, which alters the propagation characteristics of guided waves. In the present work, all delaminations were located between the two uppermost shell layers, corresponding to the interface between ply 8 and ply 9. Delaminations at other through-thickness locations were not considered, as the objective was to investigate two-dimensional damage detection and localisation. The delamination size was kept constant at $10 \times 10\,\mathrm{mm}$ and could be placed anywhere on the plate. An example delamination configuration, including a detailed view of the delaminated region, is shown in Figure 3.4.

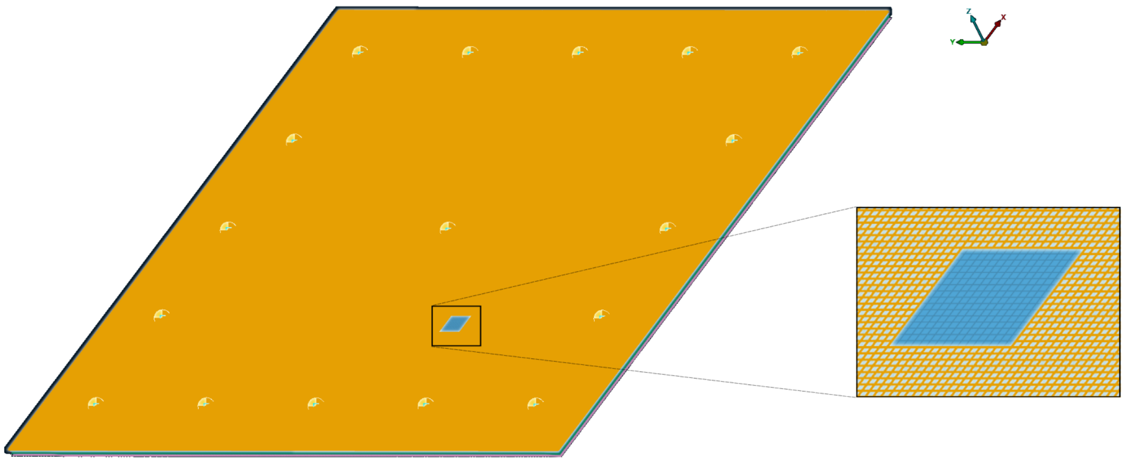

Figure 3.4: Example of a 10×10 mm delamination in the 250 mm plate, including a detailed view of the delaminated region.

To enable systematic generation of damage cases, a Python script was used to automatically generate randomised delamination positions within the laminate. The delamination location was defined by the coordinates of the delamination centre. This ensured consistent and unbiased modelling across simulations while enabling efficient creation of large, labelled datasets for supervised learning. In total, 750 unique delamination configurations were generated for the 100 mm and 250 mm plates, respectively. For the 500 mm plate, only 375 configurations were generated due to the increased computational cost associated with the larger model size.

3.1.4 Boundary conditions

Simply supported boundary conditions were applied along the plate edges. This was achieved by constraining the out-of-plane displacement of boundary nodes while allowing in-plane motion and rotations.

The choice of boundary conditions was motivated by the reflective behaviour of Lamb waves at plate edges, which may influence the signals recorded at the sensor locations. As part of the master's thesis by Lundgren and Lindström [6], a comparative study investigated the effect of clamped and simply supported boundary conditions on the measured response. The results showed that while both boundary conditions produced similar responses prior to wave reflections, clamped edges led to increased amplitudes of the reflected waves.

Since the present study considered relatively small plates and aimed to minimise the influence of boundary reflections on the recorded signals, simply supported boundary conditions were adopted throughout.

3.1.5 Excitation signal and wave generation

The excitation signal was designed to selectively excite Lamb waves at a central frequency of 100 kHz. Due to the anisotropic and dispersive nature of composite laminates, the phase velocity of guided waves is frequency-dependent and strongly influenced by the material properties and layup configuration. Consequently, the design of the excitation signal required an accurate dispersion analysis.

Solving the dispersion relations for laminated composites analytically is non-trivial. Therefore, a numerical approach was adopted using the Dispersion Calculator [20], an open-source semi-analytical finite element software that computes the dispersion characteristics for a specified material and stacking sequence. In the present work, focus was placed on the antisymmetric A_0 mode due to its sensitivity to out-of-plane defects such as delamination. The resulting dispersion curve, showing the phase velocity as a function of frequency, is presented in Figure 3.5. At 100 kHz, the phase velocity was determined to be $c_p = 1239\,\mathrm{m/s}$.

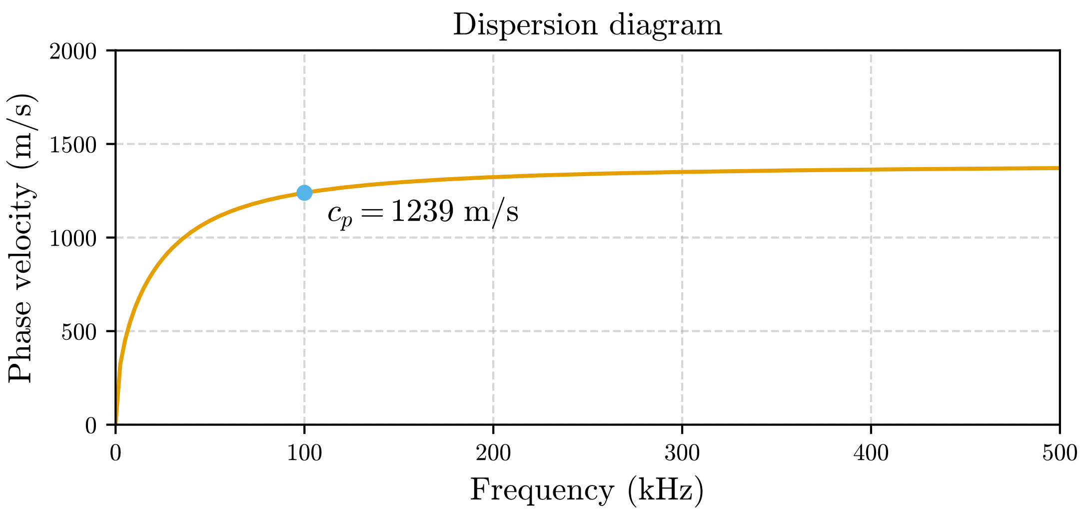

Figure 3.5: Dispersion diagram for the A_0 mode showing the phase velocity as a function of frequency.

Based on the selected excitation frequency, the input signal was defined as a five-cycle sinusoidal burst modulated by a Hann window. This type of signal provides a narrowband frequency content while minimising spectral leakage, which is essential for controlled excitation of a specific wave mode. The excitation signal $u(t)$ can be expressed as

$$u(t) = \begin{cases} A\sin(2\pi f t + \varphi)\left[\dfrac{1-\cos\left(\frac{2\pi t}{T}\right)}{2}\right], & 0 \le t \le T, \\ 0, & t > T, \end{cases} \tag{3.3}$$

where $A = 20\,\mathrm{nm}$ denotes the peak amplitude, $f = 100\,\mathrm{kHz}$ the excitation frequency, $T = 5/f$ the duration of the five-cycle burst, and φ represents a phase shift introduced to ensure symmetry of the waveform within the Hann window. The resulting excitation signal is illustrated in Figure 3.6.

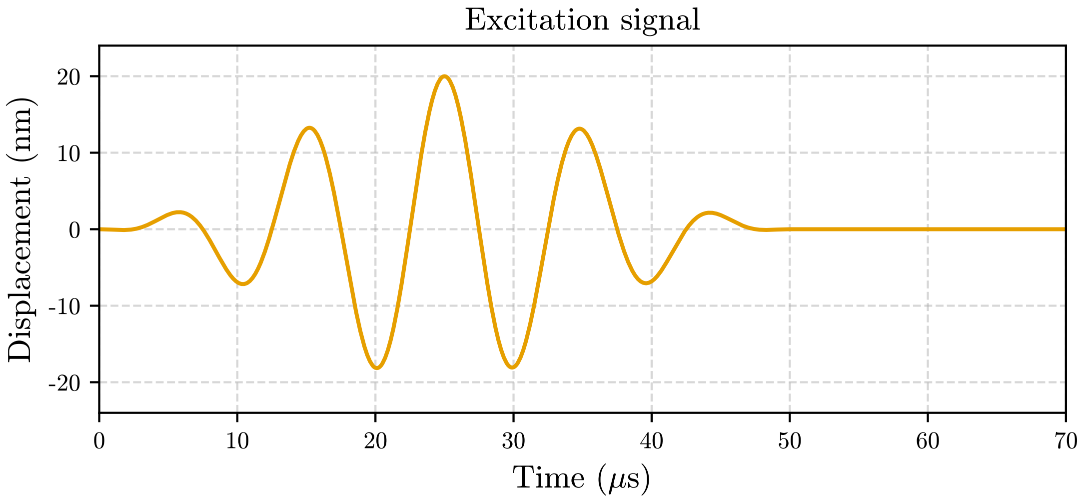

Figure 3.6: Excitation signal prescribing the out-of-plane displacement as a function of time.

The excitation was applied as a prescribed out-of-plane nodal displacement at a selected actuator node, representing an idealised piezoelectric transducer. Multiple sensor nodes were distributed across the structure, where the resulting time-dependent displacement signals were recorded. During each simulation, one node acted as the actuator while the remaining nodes served as receivers. The sensor placement is described in more detail in Section 3.1.8.

3.1.6 Mesh convergence

When modelling thin-walled structures with shell elements, excessively small in-plane element dimensions relative to the shell thickness may lead to numerical locking effects and artificially stiff behaviour [15], [21]. However, for Lamb wave propagation analyses, this guideline is often relaxed, as sufficient spatial resolution of the propagating wave is required. A common criterion is to use at least 10 elements per wavelength [13].

For an excitation frequency of 100 kHz and a phase velocity of 1239 m/s in the composite material, the corresponding wavelength was 12.39 mm. This resulted in a required element size of approximately 1.24 mm to satisfy the resolution criterion. Although this ensures adequate spatial resolution of the wave, it does not guarantee numerical convergence of the solution.

A mesh convergence study was therefore carried out to determine an appropriate element size. The study was performed on the 100 mm plate with a propagation distance of 50 mm between the actuator node and the receiver node. The mesh was successively refined by reducing the element size by a factor in the range of

1.5 to 2 between consecutive mesh levels, while ensuring that the plate dimensions remained divisible by the element size and thus permitted a structured quadrilateral mesh. Figure 3.7 shows the nodal displacement recorded at the receiver node for six different mesh sizes, h.

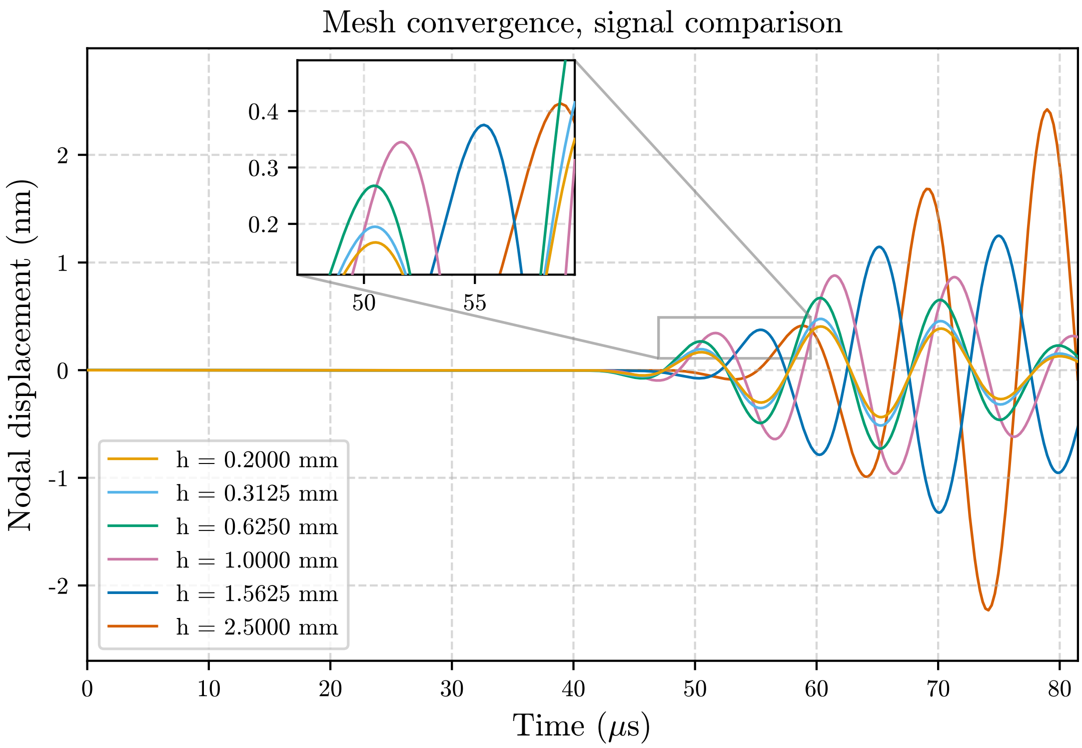

Figure 3.7: Comparison of receiver node displacement signals for six different element sizes, h. The zoomed view highlights the first significant peak of each signal.

Although clear differences between the signals were observed, it was not immediately evident at which mesh size the solution could be considered converged. To quantify convergence, the peak amplitude and the arrival time of the first wave peak were evaluated for each signal.

The relative convergence measures of the peak amplitude, u_{conv}, and the arrival time, t_{conv}, are defined in (3.4). The corresponding convergence behaviour is illustrated in Figure 3.8. $u_{\max}$ was defined as the maximum absolute value of the signal, and t_{arr} was defined as the time corresponding to the first significant peak in the displacement signal. For each mesh size, the convergence was calculated in relation to a reference value, which in this case was simply given by the smallest evaluated mesh size.

$$u_{\text{conv}} = \frac{|u_{\max,h} - u_{\max,ref}|}{u_{\max,ref}}, \qquad t_{\text{conv}} = \frac{|t_{\text{arr},h} - t_{\text{arr},ref}|}{t_{\text{arr},ref}} \tag{3.4}$$

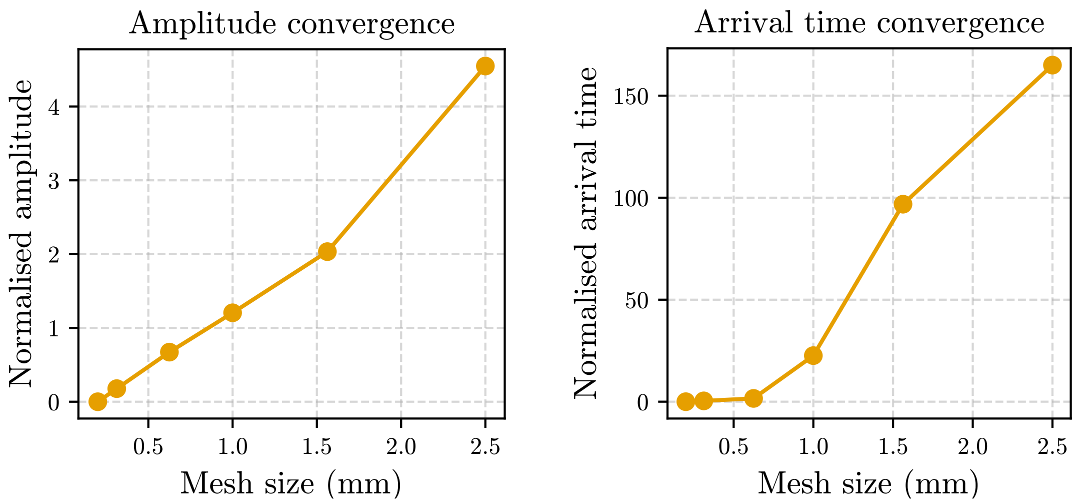

Figure 3.8: Relative convergence of peak amplitude, u_{conv}, (left) and arrival time, t_{conv}, (right) with respect to the finest mesh as reference.

From Figure 3.8, it can be observed that the amplitude converges more slowly with mesh refinement and does not exhibit clear asymptotic behaviour within the investigated range. In contrast, the arrival time converges rapidly with mesh refinement. For element sizes of 0.625 mm and below, the relative error in arrival time remains below 0.2%, indicating that the wave propagation speed is accurately captured. This observation is further supported by the calculated phase velocity. For an element size of 0.625 mm, the phase velocity was calculated as 1120 m/s, corresponding to a deviation of less than 10% from the theoretical value obtained from the dispersion analysis. Although this discrepancy is not negligible, the arrival time itself was effectively converged relative to the finest mesh and is therefore considered sufficiently accurate for the objectives of the present study, where relative changes in the sensor signals are of greater interest than an exact prediction of wave speed.

For the present application, accurate prediction of wave arrival time was considered more critical than peak amplitude. This is because the primary objective was to correctly capture wave propagation characteristics such as phase velocity and time-of-flight, which are directly related to the arrival time. Furthermore, the machine learning workflow relied on standardised sensor signals, meaning that the absolute amplitude scale was not preserved and therefore did not constitute the primary source of information available to the models. In contrast, temporal features such as wave arrival times, phase shifts, and scattering-induced distortions remained intact after preprocessing. Amplitude predictions are also generally more sensitive to numerical dispersion, local discretisation effects, and boundary interactions, and therefore often require finer spatial resolution to achieve the same level of convergence as phase-related quantities [22], [23].

Furthermore, the computational cost increases significantly with decreasing element size, as the number of elements scales with h^{-2} for the two-dimensional shell model. Reducing the element size from 0.625 mm to 0.3125 mm would therefore result in a fourfold increase in the number of elements and a corresponding increase in computational time.

Based on these considerations, a mesh size of 0.625 mm was selected, as it provided a good balance between computational efficiency and numerical accuracy. At this mesh size, approximately 20 elements per wavelength were obtained, exceeding the commonly recommended minimum requirement. Furthermore, the arrival time was effectively converged and the resulting phase velocity remained in reasonable agreement with the dispersion analysis. Although the amplitude had not fully converged, the remaining error was considered acceptable since the subsequent machine learning analysis primarily relied on temporal signal characteristics and relative amplitude rather than absolute amplitude levels.

3.1.7 Time step

The time step in LS-DYNA was automatically determined according to (2.4), presented in Section 2.3.2. For the selected mesh size of $h = 0.625$ mm, the stable time step was estimated to approximately 0.0637 µs. When compared to the CFL stability criterion shown in (2.3), this time step corresponded to a maximum Courant number of approximately 0.126. This implies that the propagating wave required roughly eight time increments to traverse a single element.

Although this time step was conservative, it satisfied the CFL criterion and provided a substantial stability margin. The automatically calculated time step in LS-DYNA was therefore adopted throughout the study.

3.1.8 Sensor placement and data acquisition

To enable consistent acquisition of guided wave responses for damage detection and localisation, a fixed sensor network was defined for each plate configuration. For all plate sizes considered in this work, the actuator node was positioned at the geometric centre of the plate. This central placement provided a symmetric excitation source, promoting uniform wave propagation in all in-plane directions and reducing directional bias in the generated dataset.

A total of 16 receiver nodes were distributed symmetrically around the plate in a square pattern, positioned 25 mm inward from each plate edge. This arrangement ensured that the sensors were located sufficiently far from the plate boundaries for the initial wave burst to reach the receivers before significant boundary reflections occurred, while still providing broad spatial coverage. The sensor layout for the 250 mm plate is illustrated in Figure 3.9. In addition to the full 16-sensor configuration, a reduced 8-sensor configuration was also investigated in the machine learning analysis. The reduced configuration consisted of every second sensor in the network (sensors 1, 3, 5, 7, 9, 11, 13, and 15), allowing the influence of sensor density on damage detection and localisation performance to be evaluated.

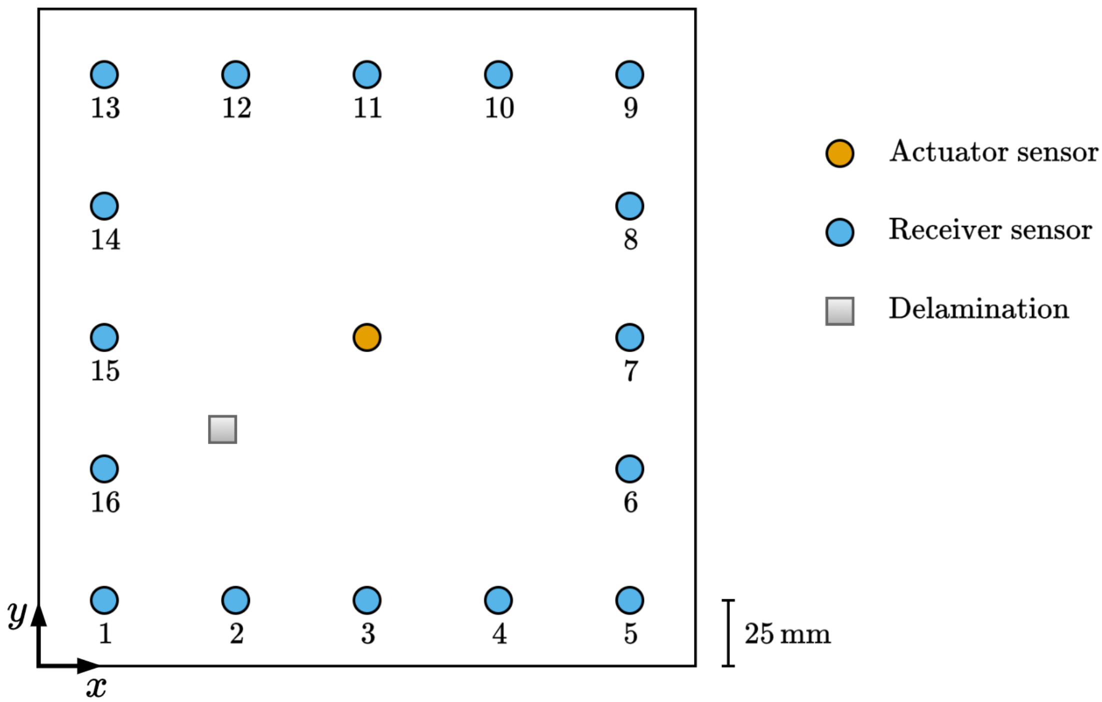

Figure 3.9: Sensor configuration for the 250 mm plate, showing the central actuator node, 16 receiver nodes, and an example delamination location.

During each simulation, the central node acted as the excitation source through the prescribed displacement signal described in Section 3.1.5, while all receiver nodes recorded time-dependent displacement responses. The total simulation time was chosen to allow the initial wave packet to propagate past all sensors, reflect from the plate boundaries, and return to the sensor locations. Consequently, the signal duration differed between the plate sizes. Simulation times of 100 µs, 200 µs, and 367 µs were used for the 100 mm, 250 mm, and 500 mm plates, respectively. Nodal displacements were recorded at every simulation time step. For the adopted mesh size, this resulted in a temporal resolution of approximately 0.064 µs, as discussed in Section 3.1.7. The recorded signals were extracted over the full simulation duration and stored for subsequent analysis.

The resulting dataset therefore consisted of multiple time-series signals for each delamination scenario and the baseline signal from the undamaged configuration. Each sample contained the dynamic response measured at all receiver locations. This systematic sensor configuration enabled both damage detection and localisation while facilitating efficient generation of structured, labelled datasets for supervised machine learning.

3.2 Machine learning methodology

The overall machine learning methodology is illustrated in Figure 3.10. The problem was formulated as a two-stage task consisting of damage detection followed by damage localisation. In the first stage, a binary classification model was trained to determine whether a given set of sensor signals corresponded to an undamaged plate or a plate containing a delamination. In the second stage, only samples identified as damaged were passed to a localisation model, which predicted the position of the delamination within the plate.

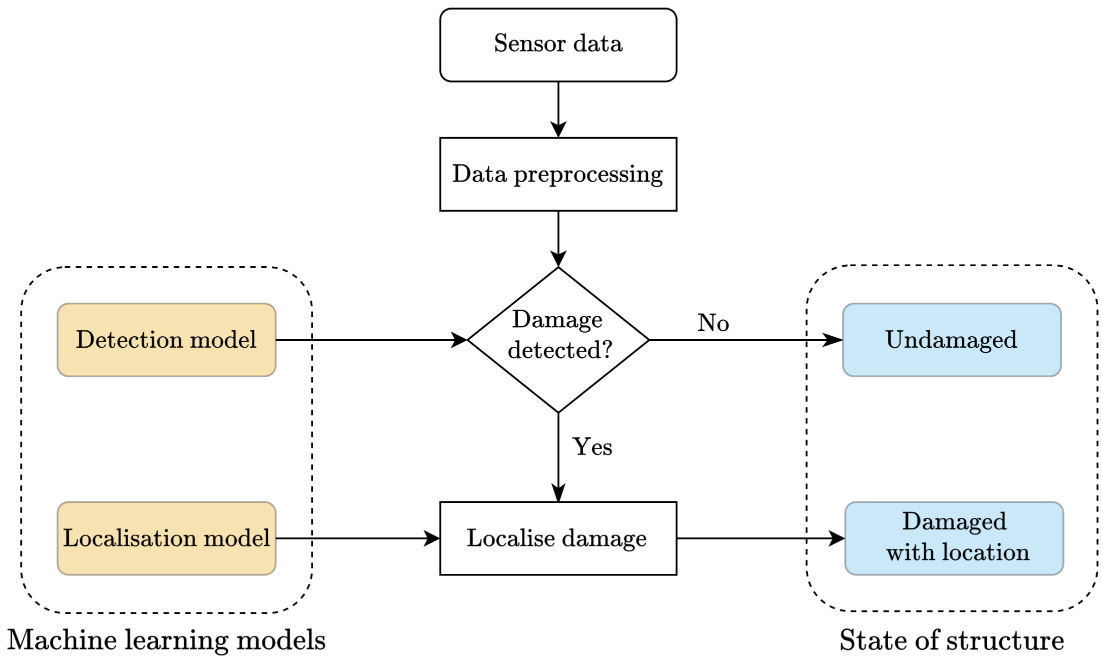

Figure 3.10: Overview of the machine learning methodology. A binary classification model is first used to determine whether a delamination is present. Samples classified as damaged are subsequently passed to a localisation model that predicts the delamination position.

3.2.1 Data augmentation

Two data augmentation techniques were employed to enrich and artificially enlarge the dataset. The first technique exploits the 180° rotational symmetry of the composite plate. By rotating the damage locations accordingly and permuting the corresponding sensor outputs, the number of unique damage scenarios can effectively be doubled. For example, the response from sensor 5 can be exchanged with that of sensor 13 after rotation (see Figure 3.9). Using this approach, the number of damage scenarios was increased from 750 to 1500 (375 to 750 for the 500 mm plate) without requiring additional computationally expensive simulations.

The second augmentation technique involved the addition of noise to the original signals. Although the dataset contains 1500 distinct damage scenarios, only a single baseline signal exists, since the explicit LS-DYNA simulations are deterministic and therefore produce identical results for a given setup. To obtain a balanced dataset, the baseline signal was first replicated 1500 times and assigned independent noise realisations, resulting in the same number of baseline samples as damage samples. Thereafter, independent noise was added to each delamination sample. This introduces realistic measurement variability and improves the robustness and generalisation capability of the machine learning models (more on noise addition in Section 3.2.2).

3.2.2 Data splitting and preprocessing

The full dataset was partitioned into three subsets: a training set, a validation set, and a test set, with proportions of 68%, 17%, and 15%, respectively. The training set was used to update the model parameters during optimisation. The validation set was used for early stopping to mitigate overfitting. The test set was reserved for the final evaluation of the model and provides an unbiased estimate of its performance on unseen data.

To ensure the data is suitable for machine learning, a few preprocessing steps are usually needed. The original sensor responses from the 8-sensor configuration for the baseline signal on the 250 mm plate can be found in Figure 3.11.

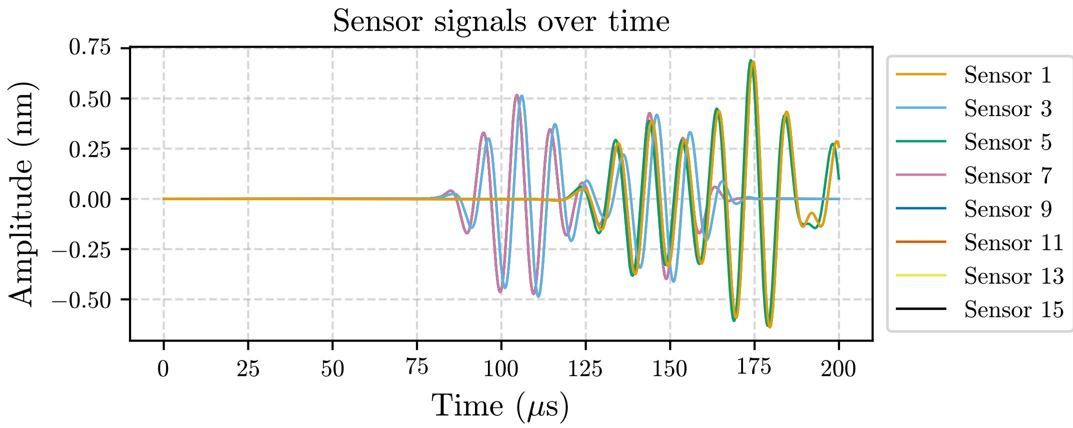

Figure 3.11: Baseline signal on the 250 mm plate from the 8-sensor configuration before data preprocessing.

The first preprocessing step consisted of applying a temporal window to the signals beginning at the time when the wave reached the nearest sensors. This removed the initial zero-valued portion of the signals. For the different plate sizes, 100 mm, 250 mm, and 500 mm, the windowing reduced the signal duration by 19 µs, 76 µs, and 171 µs, respectively.

The second step was to scale the signal features to enable stable training. The features were standardised independently for each sensor to obtain zero mean and unit standard deviation across all corresponding signals. This was accomplished by scaling each signal, x_i, according to

$$z_i = \frac{x_i - \mu_j}{\sigma_j}, \tag{3.5}$$

where μ_j and σ_j denote the mean and standard deviation, respectively, of sensor j computed from the training set and z_i is the scaled signal. The same scaling parameters were subsequently applied to the validation and test sets to prevent data leakage.

Finally, noise was added to the standardised signals. Noise samples were independently drawn from a zero-mean normal distribution with standard deviation σ, i.e. $\mathcal{N}(0, \sigma^2)$. The value of σ was determined from a prescribed signal-to-noise ratio (SNR). Expressed in decibels, the signal-to-noise ratio is defined as

$$\mathrm{SNR} = 10 \log_{10} \left(\frac{P_{\mathrm{signal}}}{P_{\mathrm{noise}}} \right), \tag{3.6}$$

where P_{signal} and P_{noise} denote the average power of the signal and noise, respectively. Assuming unit variance of the standardised signals, the corresponding standard deviation of the noise can be expressed as

$$\sigma = \frac{1}{10^{\mathrm{SNR}/20}}. \tag{3.7}$$

Figure 3.12 displays the same signals as in Figure 3.11, but after the preprocessing steps.

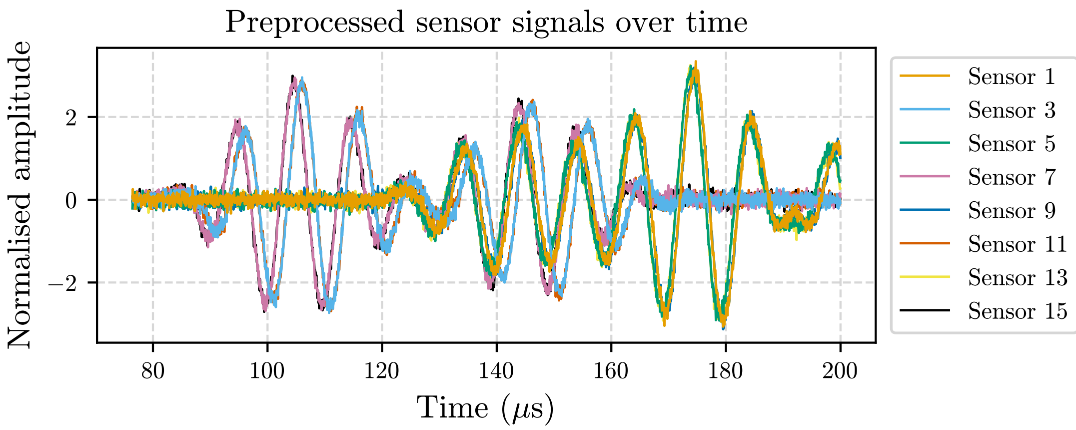

Figure 3.12: Baseline signal on the 250 mm plate from the 8-sensor configuration after data preprocessing with an SNR of 20 dB.

3.2.3 Network architecture

The proposed network architecture is a one-dimensional CNN. A key advantage of this architecture is its ability to process the time-domain signals directly and automatically extract relevant temporal features. Consequently, only limited signal preprocessing is required prior to inference.

The first part of the network consists of three convolutional layers with 64, 128, and 256 channels, respectively. All convolutional layers use a fixed kernel size of three. Each convolutional layer is followed by a ReLU activation function and a max-pooling layer with a kernel size of two.

Following the convolutional layers, the network contains a dense top comprising four fully connected layers. The first three layers contain 1024, 512, and 128 neurons, respectively. Each of these layers is followed by a ReLU activation function and a subsequent dropout layer to mitigate overfitting [24]. A dropout rate of 20% was used for all dropout layers.

Different output structures were employed for the detection and localisation tasks. Detection was formulated as a binary classification problem and therefore used a single output neuron followed by a sigmoid activation function. In contrast, localisation was treated as a regression task with two output neurons corresponding to the x- and y-coordinates, followed by a linear activation function. The architecture is summarised in Table 3.2 and visualised in Figure 3.13.

Table 3.2: One-dimensional CNN architecture for the detection task using input data from 16 sensors and 1941 data points per sensor, corresponding to the 250 mm plate. Conv1D and MaxPooling1D denote one-dimensional convolutional and max-pooling layers, respectively. For the localisation task, the final layer is modified to use a linear activation function with two output neurons instead of a sigmoid activation function with a single output neuron.

Layer	**Output Shape**
Input layer	(16, 1941)
Conv1D(ReLU, 3×1, 64)	(64, 1939)
MaxPooling1D(2×1)	(64, 969)
Conv1D(ReLU, 3×1, 128)	(128, 967)
MaxPooling1D(2×1)	(128, 483)
Conv1D(ReLU, 3×1, 256)	(256, 481)
MaxPooling1D(2×1)	(256, 250)
Flatten()	(61440)
Linear(ReLU, 1024)	(1024)
Dropout(0.20)	(1024)
Linear(ReLU, 512)	(512)
Dropout(0.20)	(512)
Linear(ReLU, 128)	(128)
Dropout(0.20)	(128)
Linear(Sigmoid,1)	(1)

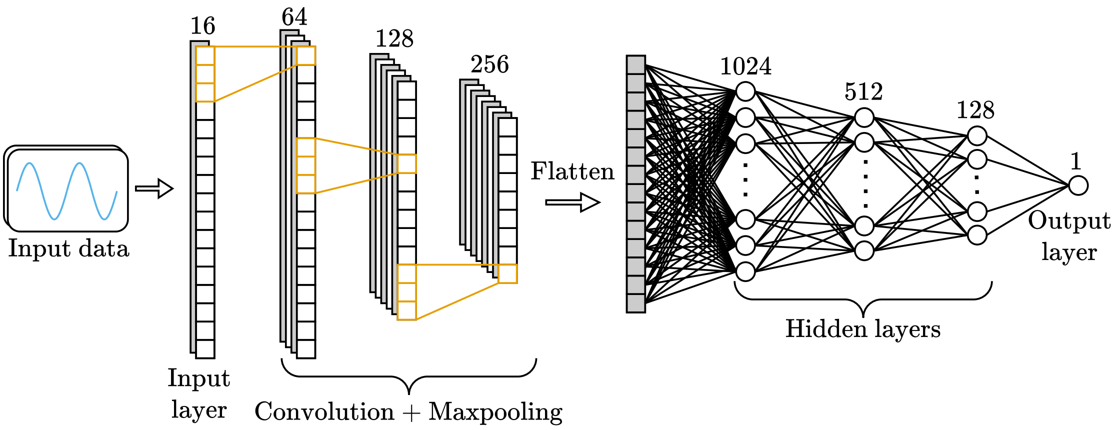

Figure 3.13: One-dimensional CNN architecture for the detection task using input data from 16 sensors. The numbers over the convolutional layers and the fully connected layers correspond to number of channels and number of neurons, respectively.

3.2.4 Network training

Two different tasks were considered: detection and localisation. The differences in network architecture between the two tasks are described in Section 3.2.3. Training was performed similarly for both tasks using the Adam optimiser with a learning rate of 0.001 and a batch size of 32. The primary differences were the choice of loss function and the number of training epochs.

For the detection task, binary cross-entropy was used as the loss function, defined as

$$L(t, \hat{t}) = -\left[t \log\left(\hat{t}\right) + (1-t) \log\left(1-\hat{t}\right)\right], \tag{3.8}$$

where t denotes the ground-truth label and $\hat{t}$ the predicted probability. The model was trained for 30 epochs.

For the localisation task, mean squared error (MSE) was employed as the loss function, and the model was trained for 45 epochs. In the two-dimensional case, the loss is given by

$$L(x, y, \hat{x}, \hat{y}) = \frac{1}{2}\left[(x-\hat{x})^2 + (y-\hat{y})^2\right], \tag{3.9}$$

where (x, y) represent the true coordinates and $(\hat{x}, \hat{y})$ the predicted coordinates.

Two experimental studies were conducted: noise variation and training dataset size variation. To obtain statistically meaningful estimates of model performance, training and evaluation were repeated across ten different data splits. For each split, noise corresponding to a range of signal-to-noise ratios (-3, 0, 3, 5, 10, 20, 30, and 40 dB) was added to the signals according to (3.7). The model was subsequently trained and evaluated for each noise level.

To investigate the influence of training dataset size on localisation and detection performance, a data scaling experiment was conducted using progressively larger subsets of the available training data. Ten different data splits were generated, and for each split the training data were divided into nine subsets, S_n, where n denotes the number of delamination samples in the subset. To ensure consistent sample composition across dataset sizes while reducing sampling-induced variance, each subset was constructed such that it was fully contained within all larger subsets:

$$S_{51} \subset S_{102} \subset S_{204} \subset S_{306} \subset S_{408} \subset S_{510} \subset S_{612} \subset S_{816} \subset S_{1020}. \tag{3.10}$$

For each subset, the model was trained using a fixed number of gradient update steps, resulting in a varying number of training epochs depending on subset size. This ensured that differences in performance originated from training set size rather than differences in optimisation effort. The total number of gradient updates was determined by training on the full dataset for 30 epochs in the detection task and 45 epochs in the localisation task. This resulted in $C_{\text{det}} = 3840$ and $C_{\text{loc}} = 5760$, where C_{det} and C_{loc} denote the total number of gradient update steps used for the detection and localisation tasks, respectively. Now let S be the number of training steps per epoch, given by $S = \left\lceil \frac{N}{B} \right\rceil$, where N represents the total number of samples in the subset and B is the batch size. Then the number of training epochs for a given subset can be determined according to

$$E_{\text{det/loc}} = \left\lfloor \frac{C_{\text{det/loc}}}{S} \right\rfloor. \tag{3.11}$$

Experiments were conducted for plate sizes of 100 mm, 250 mm, and 500 mm, using sensor configurations consisting of 8 and 16 sensors as described in Section 3.1.8.

3.2.5 Benchmark model training

To evaluate the performance of the CNN, classical machine learning algorithms were employed as benchmark models. Logistic regression was used for the binary classification task of damage detection, while ridge regression was employed for the localisation task.

In contrast to the CNN architecture, where each signal was treated as a separate channel, the signals for the classical machine learning models were concatenated into a single one-dimensional feature vector.

The regularisation parameter λ, in (2.16), for logistic regression and the penalty parameter α, in (2.11), for ridge regression were both set to one. No hyperparameter tuning was performed for these methods, as such optimisation was considered outside the scope of this thesis.

4

Results

This chapter presents the results obtained from both the finite element simulations and the machine learning models. The numerical simulation results are first evaluated to verify the physical validity of the generated dataset, after which the performance of the machine learning framework is presented for delamination detection and localisation.

4.1 Finite element simulations

This section evaluates the physical behaviour of the finite element simulations through wave field visualisation, signal comparison, and attenuation analysis.

4.1.1 Wave propagation and damage interaction

To qualitatively validate the numerical model, wave field visualisations are examined for both undamaged and delaminated configurations of the 250 mm plate. Figure 4.1 illustrates the wave propagation in the undamaged plate. The Lamb wave is excited from the centrally located actuator node and propagates radially through the laminate before reflecting at the plate boundaries.

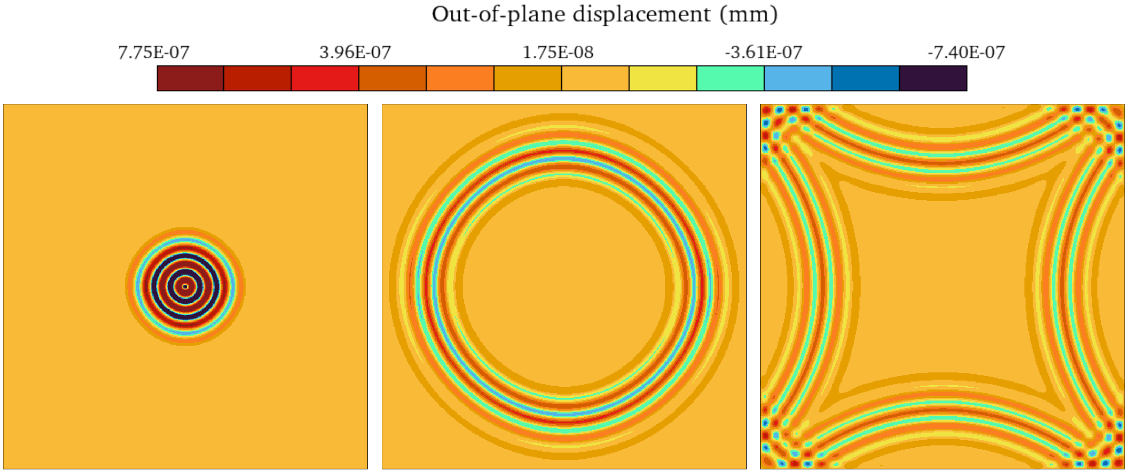

(a) 40 µs **(b)** 100 µs **(c)** 160 µs

Figure 4.1: Wave propagation in the undamaged 250 mm plate at different time instances.

Figure 4.2 shows the corresponding wave propagation for a plate containing a delamination located beneath the actuator. Compared to the undamaged case, the delamination introduces local wave scattering, reflections, and distortion of the propagating wavefront due to the loss of interlaminar continuity.

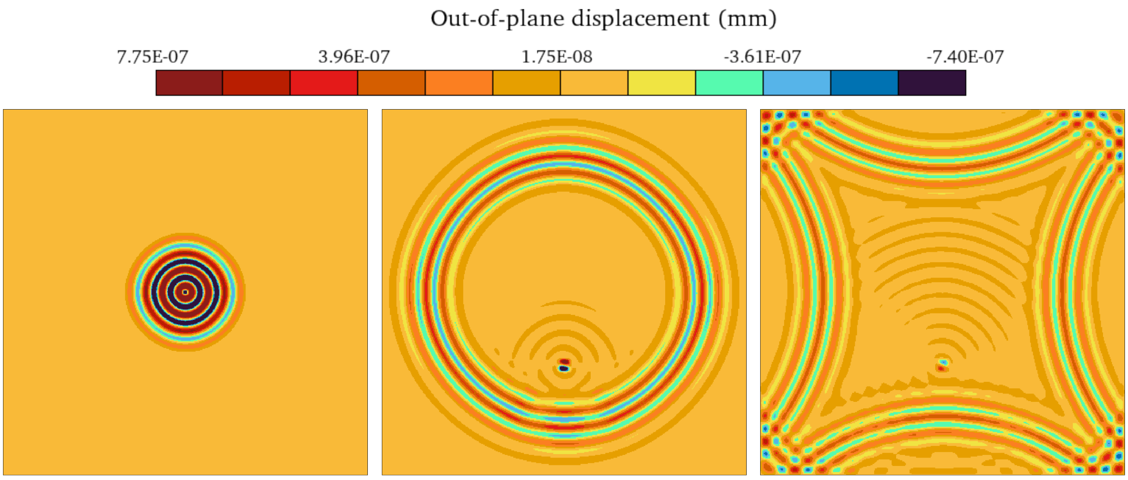

(a) 40 µs **(b)** 100 µs **(c)** 160 µs

Figure 4.2: Wave propagation in the delaminated 250 mm plate at different time instances. Delamination is located directly in between the central actuator and sensor 3.

To further investigate the influence of delamination on the measured response, the nodal displacement recorded at sensor 3 is evaluated. Figure 4.3 compares the displacement signals obtained for the undamaged and delaminated configurations. The delamination is positioned directly along the propagation path between the actuator and sensor 3, just as in Figure 4.2.

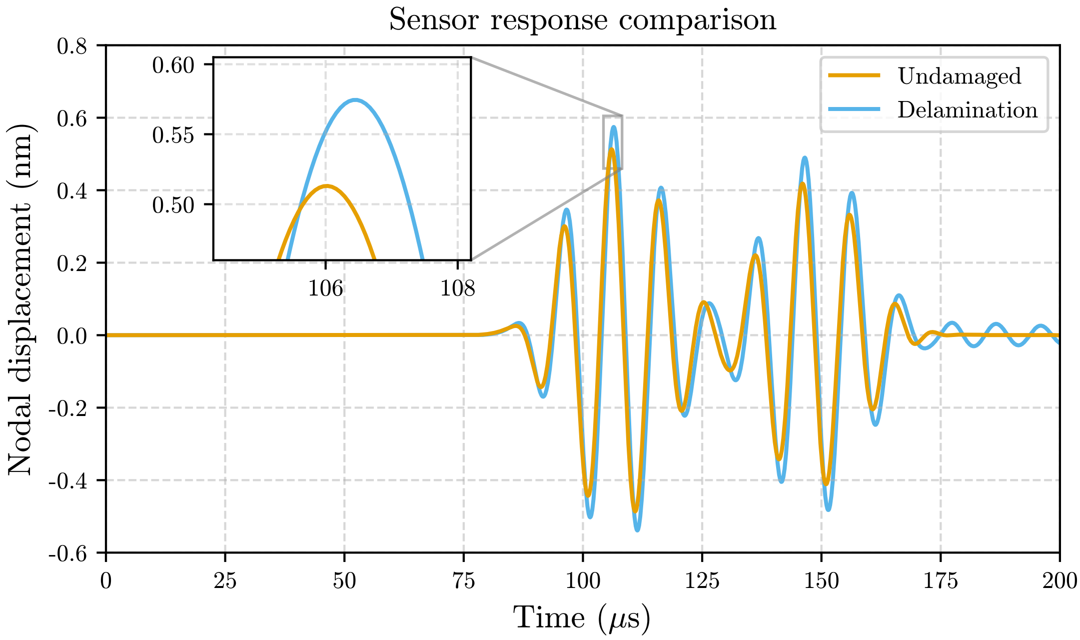

Figure 4.3: Comparison of nodal displacement signals measured at sensor 3 for undamaged and delaminated configurations.

The presence of delamination results in measurable differences in the recorded response, including changes in both signal amplitude and temporal characteristics.

4.1.2 Amplitude attenuation

The geometric attenuation of Lamb waves in a two-dimensional medium is proportional to $1/\sqrt{r}$, where r denotes the propagation distance from the excitation source. Consequently, the wave amplitude as a function of propagation distance can be expressed as

$$A(r) = \frac{C}{\sqrt{r}}, \tag{4.1}$$

where C is a proportionality constant accounting for factors other than geometric spreading.

To validate that the simulated wave propagation exhibits the expected geometric attenuation, a verification study was conducted using ten sensor nodes positioned at 25 mm intervals from the excitation source, corresponding to propagation distances ranging from 25 mm to 250 mm.

At the reference distance $r_0 = 25\,\text{mm}$, the measured amplitude is defined as

$$A_0 = A(r_0) = \frac{C}{\sqrt{r_0}}. \tag{4.2}$$

By normalising both amplitude and propagation distance with respect to the reference measurement, the relative amplitude attenuation can be expressed independently of the proportionality constant:

$$\frac{A(r)}{A_0} = \frac{1}{\sqrt{r/r_0}}. \tag{4.3}$$

Figure 4.4 compares the normalised measured amplitudes with the theoretical geometric attenuation model.

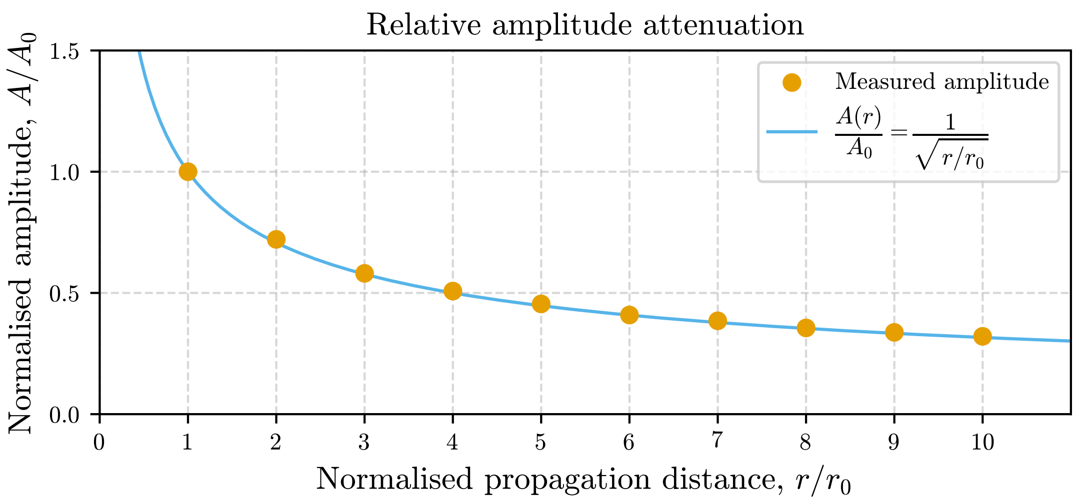

Figure 4.4: Comparison between simulated amplitude attenuation and the theoretical geometric attenuation model.

The measured amplitudes closely follow the theoretical attenuation trend, indicating that the simulated Lamb wave propagation exhibits physically consistent behaviour with respect to geometric spreading.

4.2 Machine learning results

This section presents the machine learning results for both the detection and localisation tasks. In each case, the performance of the CNN is first compared with that of the corresponding benchmark model on the 250 mm plate using the 16-sensor configuration. The influence of sensor configuration is then investigated by comparing results obtained using 8 and 16 sensors. Finally, performance is compared across the different plate sizes, all using 16 sensors. The complementary results on the 100 mm and 500 mm plates can be found in Appendix A.

For each task, two experimental studies are presented: variation of noise level and variation of training dataset size. In the dataset scaling study, a fixed SNR of 20 dB was used. Conversely, when investigating the effect of noise level, the full training dataset was employed.

4.2.1 Delamination detection

Figure 4.5 compares the delamination detection accuracy of the CNN and logistic regression models. The solid lines represent the mean accuracy across the ten runs, while the shaded regions indicate ±1 standard deviation.

In the left plot, detection accuracy increases with decreasing noise levels (i.e. increasing SNR) for both models. The CNN outperforms logistic regression across lower noise levels and achieves near-perfect accuracy for SNR values of 20 dB and above. However, performance degrades substantially at 10 dB, where the variance also increases considerably, indicating large performance differences between individual runs. Logistic regression exhibits more stable behaviour across the investigated noise range, with consistently smaller variances, although the achieved accuracy remains lower than that of the CNN at lower noise levels.

Similar trends are observed for both models in the data scaling experiment shown in the right plot. Across all dataset sizes, the CNN achieves approximately eight to ten percentage points higher mean accuracy than logistic regression. CNN performance begins to saturate beyond 510 delamination samples, whereas logistic regression continues to show gradual improvements with increasing dataset size.

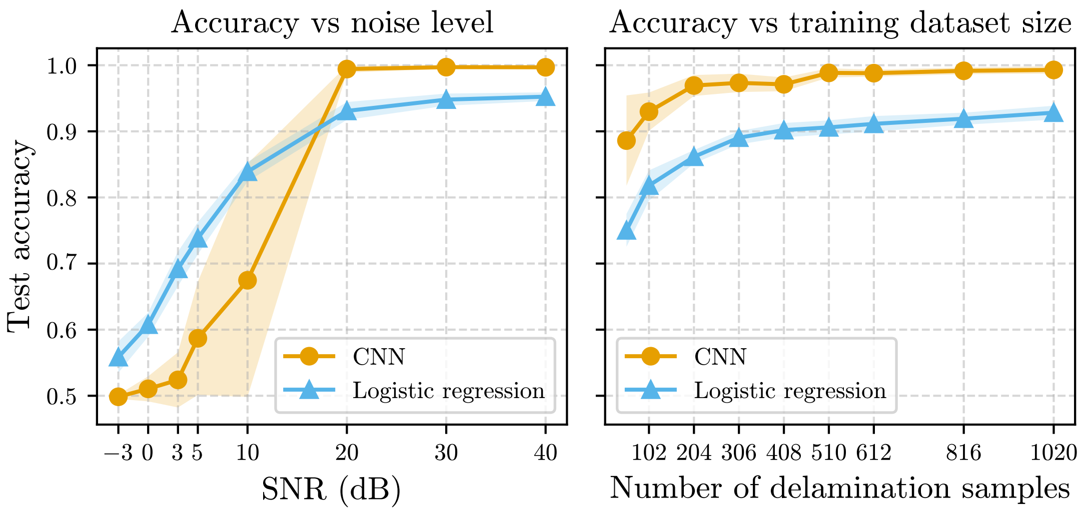

Figure 4.5: Comparison of delamination detection accuracy for the CNN and logistic regression models on the 250 mm plate using 16 sensors. Solid lines represent the mean accuracy across ten runs, while shaded regions indicate ±1 standard deviation. The CNN achieves near-perfect accuracy at high SNR levels and consistently outperforms logistic regression in the data scaling experiment. Logistic regression exhibits more stable variance across the investigated noise levels.

Figure 4.6 presents a comparison of delamination detection performance using 8 and 16 sensors on the 250 mm plate. Overall, both sensor configurations yield nearly identical results. At an SNR of 10 dB, the 16-sensor configuration exhibits lower mean accuracy than the 8-sensor configuration, although both cases are associated with large variances. A slight reduction in accuracy for the 16-sensor configuration is also observed for smaller training dataset sizes.

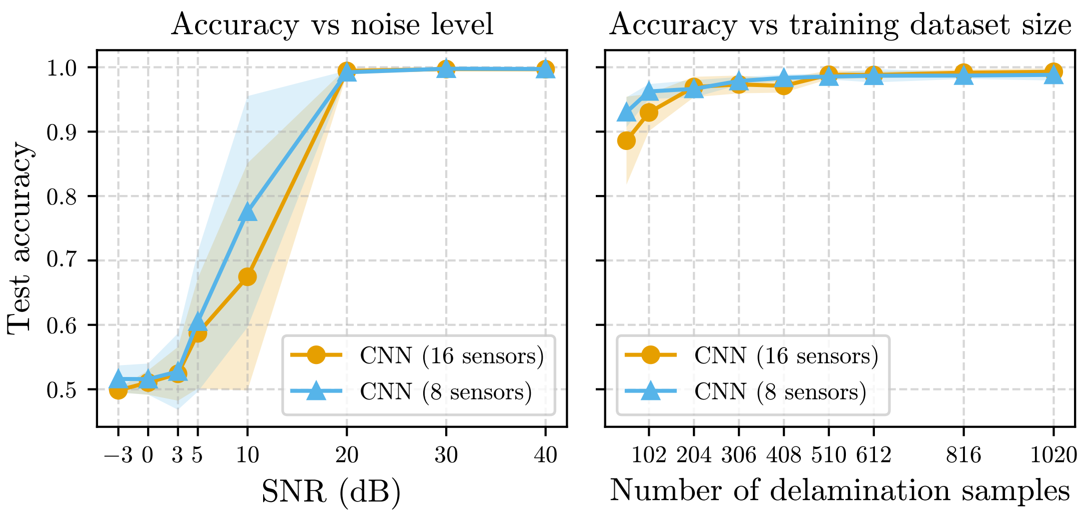

Figure 4.6: Comparison of delamination detection accuracy for the CNN model on the 250 mm plate using 8, and 16 sensors, respectively. Solid lines represent the mean accuracy across ten runs, while shaded regions indicate ±1 standard deviation. Near identical performance using the 8-sensors or 16-sensors configuration.

Figure 4.7 presents a comparison of the delamination detection accuracy of the CNN model for three different plate sizes, using the 16-sensor configuration. The results in the left plot indicate that the model exhibits greater robustness to increasing noise levels for smaller plate sizes, with the mean accuracy on the 100 mm plate remaining above 80% down to an SNR of 5 dB. For the 500 mm plate, the mean accuracy increases at an SNR of 20 dB, but this is accompanied by a substantial variance. The large variance observed for certain noise levels, for all three plate sizes, was found to originate from occasional runs with failed training convergence. It should also be noted that, for the 500 mm plate, only half as many training samples are available compared with the other two plate sizes.

In the data-scaling experiment shown in the right plot, the trends for the 100 mm and 250 mm plates are nearly identical. In contrast, for the 500 mm plate, no clear performance improvement is observed when the number of delamination samples is increased. Moreover, the large variance observed for all results on the 500 mm plate suggests unstable performance across different runs.

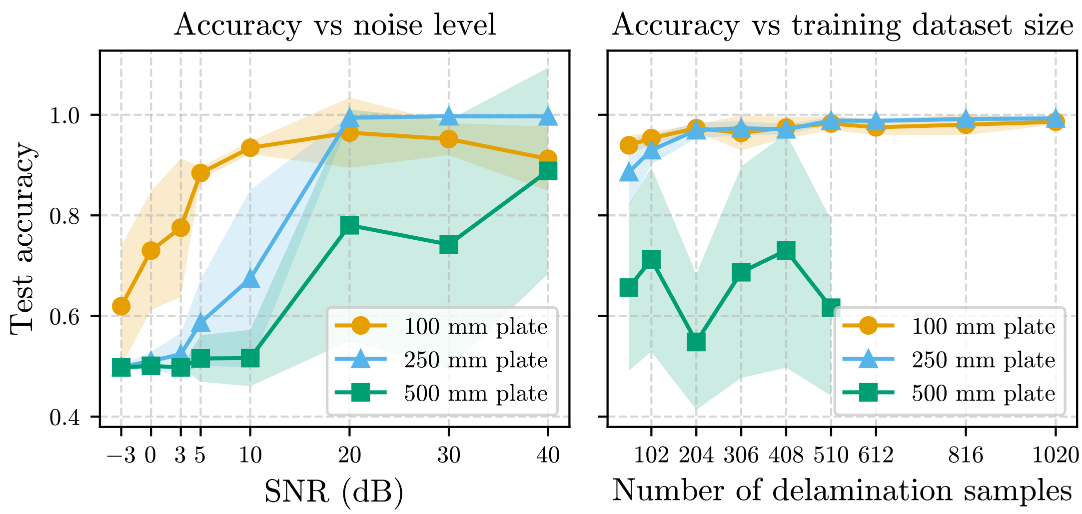

Figure 4.7: Comparison of delamination detection accuracy for the CNN model on three different plate sizes using 16 sensors. Solid lines represent the mean accuracy across ten runs, while shaded regions indicate ±1 standard deviation. The model exhibits greater robustness to increasing noise levels for smaller plate sizes. On the 500 mm plate the results are associated with a large variance, and no clear improvement is shown when number of delamination samples is increased.

Figure 4.8 shows the distribution of test accuracy across runs for both the CNN (orange circles) and logistic regression (blue triangles) on the 500 mm plate with 16 sensors, across varying noise levels. For the CNN, at high SNR values, two distinct populations are visible: runs with failed training convergence, which plateau at approximately 50% test accuracy, and successful runs, which exceed 95%. The CNN exhibits a clearly bimodal distribution, with runs falling into one of these two groups, while logistic regression displays a unimodal distribution. A bimodal distribution is not well characterised by a single mean and standard deviation, and this limitation should be kept in mind when interpreting the summary statistics presented in the preceding figures. That representation has nonetheless been retained, as the majority of results are unimodal; however, cases where the CNN exhibits large variance are likely indicative of this bimodal behaviour rather than a gradual spread of performance.

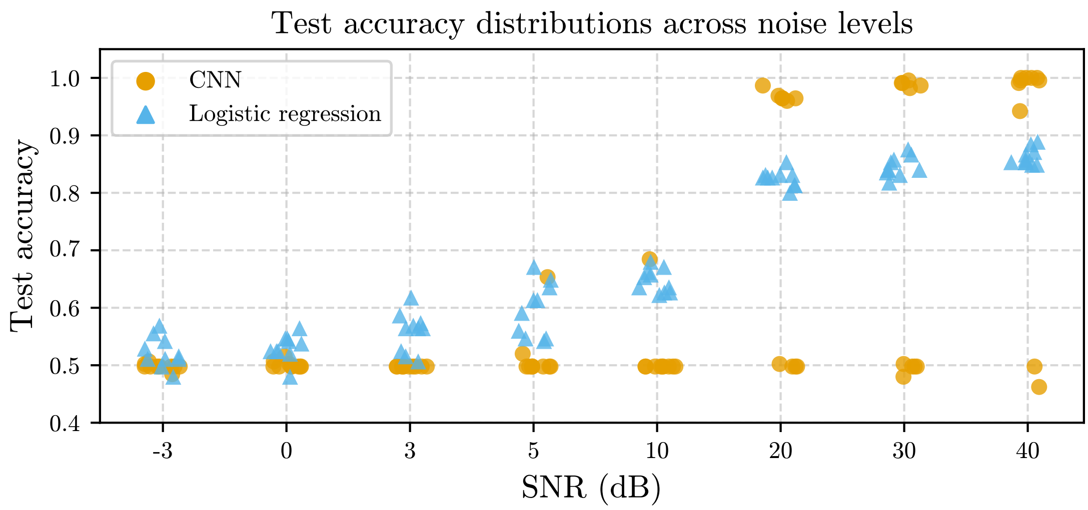

Figure 4.8: Comparison of delamination detection accuracy for the CNN and logistic regression models on the 500 mm plate using 16 sensors. Each marker corresponds to the test accuracy obtained from a single run. The CNN displays a bimodal distribution, with results clustering either at high accuracy or at approximately 50% accuracy, while logistic regression exhibits a unimodal distribution.

4.2.2 Delamination localisation

To aid interpretation of the localisation results, it should be noted that the reported MSE values are calculated using coordinates normalised by the plate dimensions. Consequently, the square root of the MSE corresponds to the localisation error expressed as a fraction of the plate size. For example, an MSE of 0.0025 corresponds to a root mean squared error (RMSE) of 0.05, equivalent to a localisation error of 5% of the plate length. This corresponds to 5 mm, 12.5 mm, and 25 mm for the 100 mm, 250 mm, and 500 mm plates, respectively.

Figure 4.9 compares the delamination localisation performance of the CNN and ridge regression models. The solid lines represent the mean MSE across the ten runs, while the shaded regions indicate ± 1 standard deviation.

For the CNN, there is a monotonic decrease in MSE as the noise level is reduced, as seen in the left plot. In contrast, for ridge regression the error begins to increase beyond an SNR of 10 dB, accompanied by an increase in variance. For the CNN, the reduction in MSE saturates at an SNR of 20 dB, and as the noise level decreases a pronounced performance gap emerges between ridge regression and the CNN.

In the data scaling experiment shown in the right plot, the MSE for the CNN decreases rapidly as the number of delamination samples in the training set increases. However, the rate of improvement diminishes once the training set exceeds 204 samples, indicating a saturation effect. For ridge regression, the trend is less pronounced: there is a modest reduction in MSE when nearly the entire dataset is used, but all corresponding values exhibit substantial variance, obscuring a clear scaling behaviour.

The performance for ridge regression differs substantially depending on plate size. On the 100 mm plate, variance remains stable across all noise levels and the error continues to decrease monotonically (see Figure A.10). On the 500 mm plate, the effect of increased variance is even more pronounced than on the 250 mm plate, with performance degrading significantly at low noise levels (see Figure A.13).

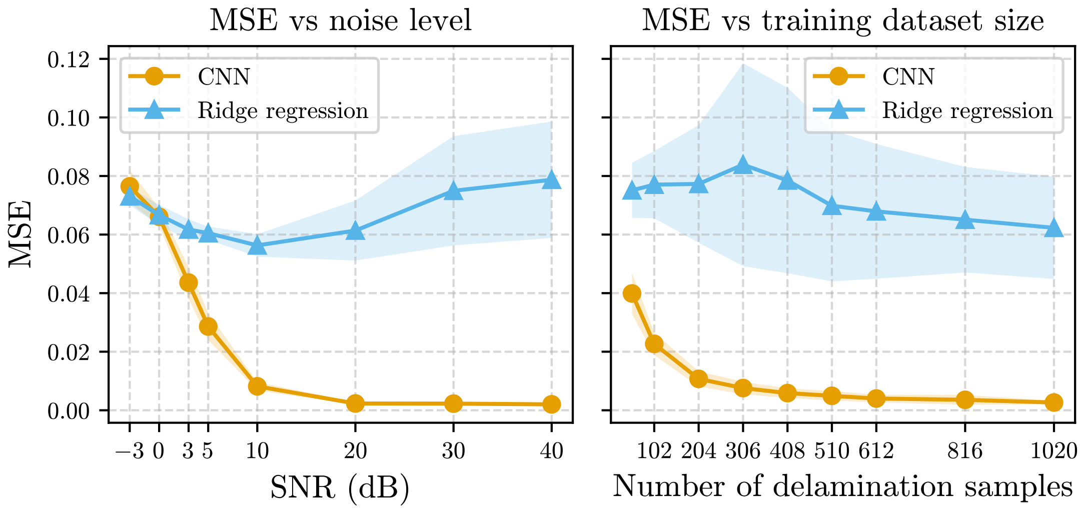

Figure 4.9: Comparison of delamination localisation MSE for the CNN and ridge regression models on the 250 mm plate using 16 sensors. Solid lines represent the mean MSE across ten runs, while shaded regions indicate ±1 standard deviation. On the 250 mm plate an MSE of 0.0025 corresponds to an RMSE of 12.5 mm in physical units. The MSE for the CNN decreases rapidly and outperforms ridge regression for almost every noise level. The CNN shows a rapid decrease in MSE for an increasing amount of training data.

Figure 4.10 illustrates the interpretation of MSE as a performance metric for the localisation task. Two different noise realisations are shown for a given test instance, corresponding to SNR values of −3 dB and 40 dB, respectively. The figure compares the predicted delamination positions produced by the CNN with the true positions. The x-axes represent the true coordinates, while the y-axes show the predicted x- and y-coordinates. Normalised coordinates are utilised, indicating that $(0, 0)$ corresponds to the bottom left corner of the plate, while $(1, 1)$ corresponds to the top right corner.

In the ideal case, all markers would lie on the dashed diagonal line, corresponding to perfect predictions. The orange circles represent predictions obtained under heavy noise conditions (−3 dB), whereas the blue triangles correspond to predictions at low noise levels (40 dB). Predictions obtained at higher SNR align substantially better with the true positions, resulting in significantly lower localisation error. The corresponding MSE values are 0.076 and 0.0018 for the high- and low-noise cases, respectively.

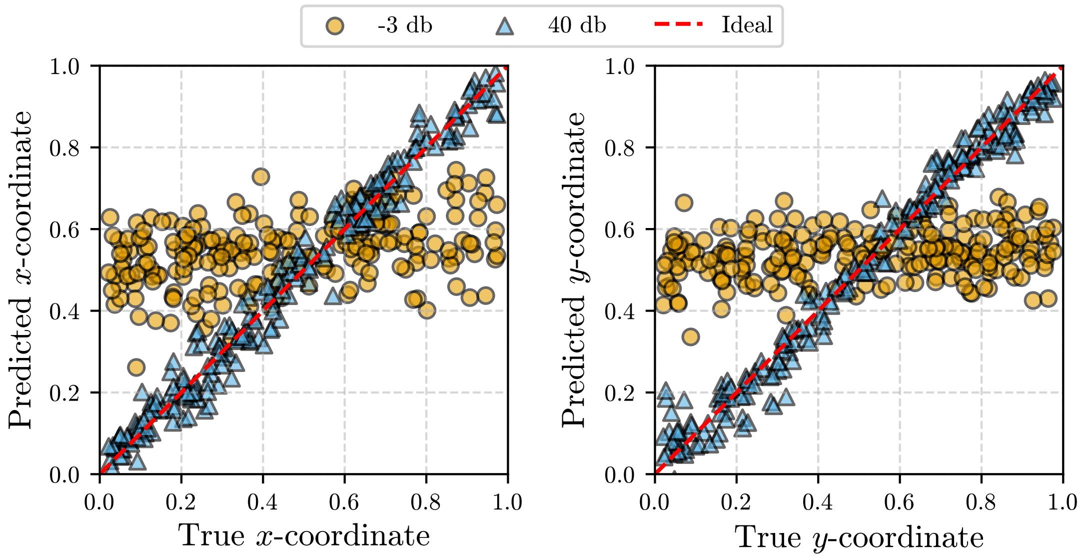

Figure 4.10: Predicted delamination positions from the CNN for two different noise realisations on the 250 mm plate using 16 sensors. Predictions obtained at higher SNR align substantially better with the true positions. The MSE values are 0.076 and 0.0018 for -3 dB and 40 dB, respectively.

Figure 4.11 presents a comparison of delamination localisation performance using 8 and 16 sensors on the 250 mm plate. The 16-sensor configuration demonstrates greater robustness at intermediate noise levels (3 dB to 10 dB), while performance is essentially identical at both lower and higher noise levels. This advantage is not observed on the 100 mm and 500 mm plates, where performance is essentially identical across both sensor configurations regardless of noise level (see Figure A.14 and Figure A.15).

In the data scaling experiment shown in the right plot, both configurations exhibit nearly identical trends, although the localisation error remains consistently slightly lower for the 16-sensor configuration.

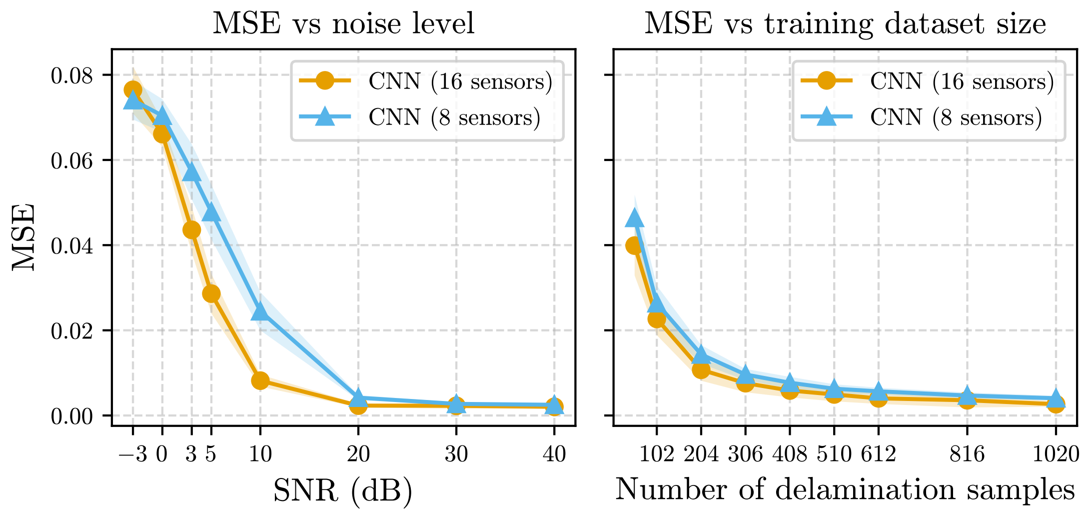

Figure 4.11: Comparison of delamination localisation MSE for the CNN model on the 250 mm plate using 8, and 16 sensors, respectively. Solid lines represent the mean MSE across ten runs, while shaded regions indicate ±1 standard deviation. Greater robustness at intermediate noise levels for the 16-sensor configuration.

Figure 4.12 presents a comparison of the delamination localisation MSE of the CNN model for three plate sizes using the 16-sensor configuration. Localisation performance was evaluated in normalised coordinate space, meaning that equal MSE corresponds to equal relative localisation accuracy across plate sizes. Results in the left plot indicate that the model exhibits greater robustness to increasing noise for smaller plate sizes, with the 100 mm plate consistently achieving the lowest MSE. For all plate sizes, the MSE increases noticeably below an SNR of 10 dB, indicating reduced localisation accuracy under high noise conditions.

At higher SNR levels (20 dB to 40 dB), the 100 mm and 250 mm plates exhibit nearly identical errors, whereas the MSE for the 500 mm plate is notably higher. It should also be noted that only half as many training samples were available for the 500 mm plate compared with the two smaller plate sizes.

In the data scaling experiment shown in the right plot, similar trends are observed across all plate sizes. Differences between the 100 mm and 250 mm plates remain consistently small, while the 500 mm plate exhibits slightly higher localisation error throughout.

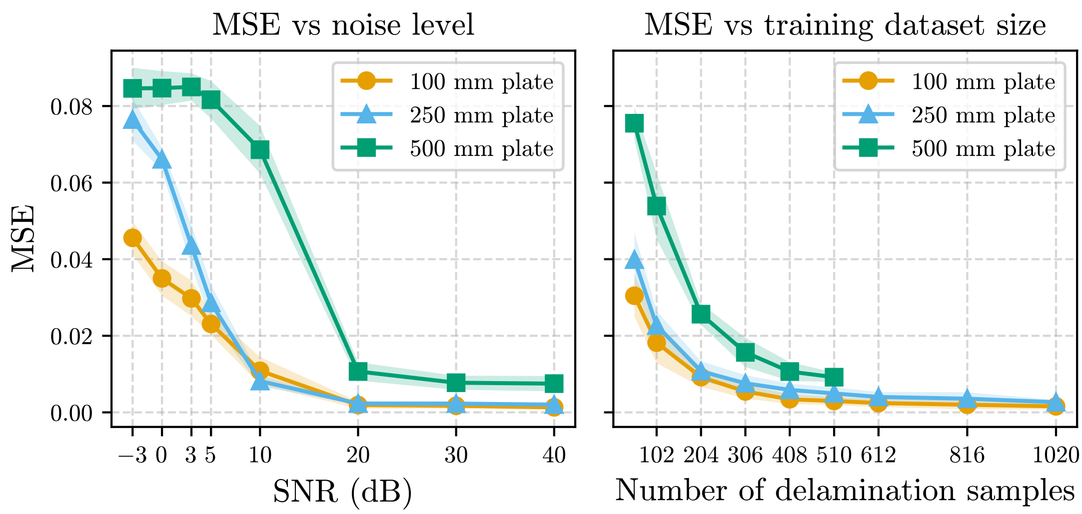

Figure 4.12: Comparison of delamination localisation MSE for the CNN model on three different plate sizes using 16 sensors. Solid lines represent the mean MSE across ten runs, while shaded regions indicate ±1 standard deviation. The model exhibits greater robustness to increasing noise levels for smaller plate sizes. Similar trends for all plate sizes as dataset size increases.

Figure 4.13 presents the localisation error as a function of sensor spacing. While the same sensor configurations, consisting of either 8 or 16 sensors, were used for all plates, the different plate dimensions lead to varying distances between neighbouring sensors. To ensure equal training conditions, 510 delamination samples were used for all plate sizes. The results indicate a trend of increasing localisation error with increasing sensor spacing.

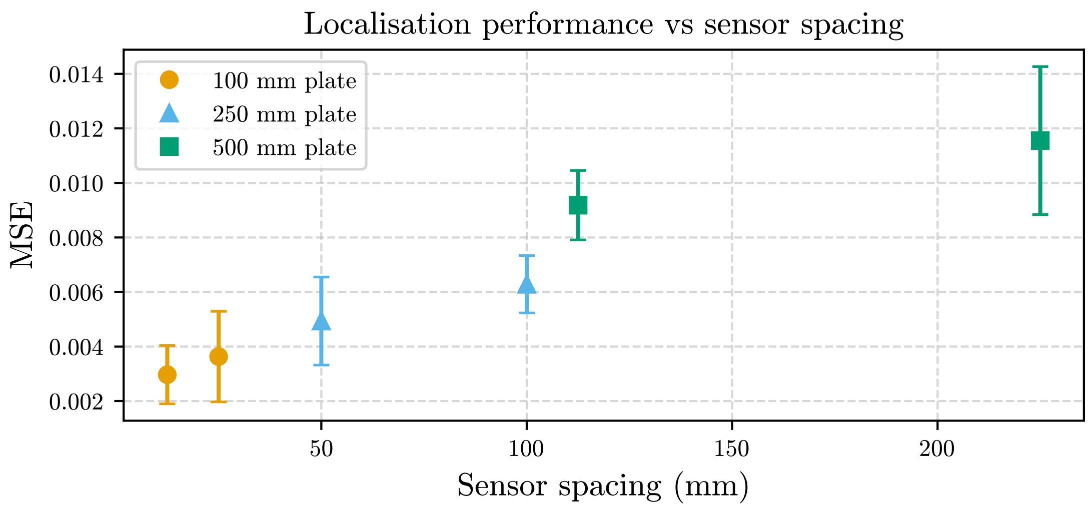

Figure 4.13: Localisation error for the CNN in relation to sensor spacing. Markers represent the mean MSE across ten runs, while error bars indicate ±1 standard deviation.

5

Discussion

This chapter discusses the results presented in Chapter 4 in relation to the adopted methodology and the limitations of the study.

5.1 Numerical modelling and wave propagation

The wave field visualisations demonstrated the expected propagation characteristics of guided waves in a plate structure. In the undamaged configuration (see Figure 4.1), the wavefront propagated radially from the actuator before interacting with the plate boundaries. Introducing a delamination (see Figure 4.2) resulted in local scattering and distortion of the wavefront, producing measurable differences in the recorded sensor signals.

This behaviour is also reflected in the sensor response shown in Figure 4.3. Compared with the undamaged plate, the delaminated configuration exhibits both amplitude variations and temporal changes in the recorded signal. Interestingly, the peak amplitude is larger in the delaminated case. While one might intuitively expect the amplitude to decrease due to wave scattering at the delamination, the observed increase is likely caused by the interaction between the incident wave and wave components scattered by the damage. Depending on their relative phase when reaching a sensor location, constructive interference can locally increase the measured amplitude, whereas destructive interference may lead to a reduction. Although the precise mechanism was not investigated in detail, the observed behaviour is consistent with such wave superposition effects. Regardless of whether the local amplitude increases or decreases, the presence of the delamination introduces measurable changes to the recorded signal that can be exploited for damage detection and localisation.

Further confidence in the numerical model is provided by the attenuation study presented in Section 4.1.2. The simulated amplitude decay followed the theoretical geometric attenuation relationship proportional to $1/\sqrt{r}$, indicating that the propagating Lamb waves exhibit physically reasonable spreading behaviour. However, agreement with the theoretical attenuation trend alone does not guarantee complete correspondence with real structures, as the model neglects several physical effects such as material damping, manufacturing imperfections, environmental influences, and the electromechanical behaviour of piezoelectric transducers.

To enable generation of large datasets within a reasonable computational time, several modelling simplifications were introduced. The laminate was represented by four shell layers rather than explicitly modelling all 32 plies, reducing the computational cost while still permitting representation of interlaminar damage. Similarly, the actuator was idealised through a prescribed displacement rather than a fully coupled piezoelectric model. Although these simplifications limit the physical accuracy of the simulations, they provide an efficient framework for generating large quantities of labelled data suitable for machine learning applications. In total, 1875 unique delamination configurations were simulated across three plate sizes. This is a key advantage of the simulation-based approach, as such datasets would be difficult and costly to obtain experimentally. However, because all data originate from a numerical model, the resulting machine learning models may be sensitive to modelling assumptions and would therefore require experimental validation before being applied to real SHM systems.

5.2 Delamination detection

The comparison between the CNN and logistic regression models for delamination detection indicates that the CNN performs better under favourable noise conditions. For moderate to low noise levels (SNR values of 20 dB and above), the CNN consistently achieves higher detection accuracy than logistic regression for both the 100 mm and 250 mm plates.

As the noise level increases, the features that distinguish damaged signals from baseline signals become increasingly obscured. Since the applied noise is purely additive, phase information is expected to be more robust than amplitude information: additive noise perturbs signal amplitudes directly, while phase shifts remain comparatively stable at lower SNR levels. One possible explanation for the superior performance of logistic regression at high noise levels is therefore that it relies more heavily on phase-related features, whereas the CNN may place greater emphasis on local amplitude variations, making it more sensitive to additive noise. This hypothesis is consistent with the CNN architecture employed in this study, where all convolutional layers use a kernel size of three, which is small relative to the total signal length. Such a configuration primarily captures local temporal patterns and may limit the network's ability to exploit phase information distributed over longer time intervals. A larger kernel size would increase the receptive field and could potentially improve robustness to noise, though at the cost of reduced emphasis on local features and increased computational complexity. This interpretation remains speculative, however, as the features utilised by each model were not explicitly analysed in this study.

Large variance in detection accuracy was observed for the CNN under certain conditions (see Figure 4.7), particularly for the 250 mm plate at an SNR of 10 dB, the 100 mm plate in the range −3 dB to 3 dB, and the 500 mm plate in the range 20 dB to 40 dB. Examination of individual training runs revealed that the CNN occasionally failed to converge to a meaningful solution, becoming trapped in a local minimum where training accuracy remained close to 50% and the network effectively predicted only a single class for all samples.

This behaviour was especially pronounced for the 500 mm plate, where training outcomes were strongly bimodal: individual runs either converged to test accuracies exceeding 95% or failed almost entirely (see Figure 4.8). This pattern is notable because it suggests that the optimisation landscape for the 500 mm plate contains particularly deep local minima that are difficult to escape. Qualitatively similar, though less pronounced, patterns were observed for the 100 mm and 250 mm plates, where successful runs typically achieved test accuracies between 70% and 88%, depending on the noise level.

The instability observed across plate sizes suggests that the optimisation problem becomes increasingly difficult for larger plates and under higher noise conditions. Larger plates produce higher-dimensional input signals and consequently a greater number of trainable parameters, making the optimisation process more sensitive to weight initialisation and stochastic gradient updates. A reduced number of training samples may further contribute to this behaviour for the 500 mm plate. However, this explanation is not fully supported by the data scaling experiments, where the 100 mm and 250 mm plates achieved strong performance even with relatively small datasets, while the 500 mm plate exhibited no clear improvement as dataset size increased. This discrepancy suggests that dataset size alone is insufficient to account for the instability and that architectural modifications or more extensive hyperparameter tuning may be necessary to mitigate this problem.

The model instances that do converge to meaningful solutions generally achieve higher detection accuracies than logistic regression. Under favourable conditions, the CNN consistently attains near-perfect accuracy, demonstrating that it is capable of learning highly discriminative features from the signal data. In contrast, logistic regression exhibits more stable performance across training runs, albeit at a somewhat lower accuracy. Consequently, if maximising detection accuracy is the primary objective, the CNN appears to be the more promising approach. It should be noted, however, that no hyperparameter tuning was performed for logistic regression in this study. Systematic tuning using the validation set could plausibly improve its performance, and the present results should therefore not be interpreted as establishing a definitive performance ceiling for that model.

5.3 Delamination localisation

The CNN outperforms ridge regression on the localisation task under nearly all investigated conditions. The only exception occurs at high noise levels for the 250 mm and 500 mm plates, where both models perform similarly poorly. Ridge regression generally exhibits weak performance even under conditions that would typically be considered favourable, such as low noise levels and large training datasets. This suggests that the relationship between the input signals and the delamination coordinates is not well captured by a linear model and that a more complex mapping is required.

Counterintuitively, ridge regression exhibits worse localisation performance as the noise level is reduced for both the 250 mm and 500 mm plates, with the effect becoming more pronounced for larger plate sizes. Both the mean localisation error and its variance increase at higher SNR levels, and a substantial gap between training and test errors indicates that the model is prone to overfitting. The likely mechanism is as follows: at higher SNR levels the signal features are more distinct, causing the model to fit closely to specific patterns in the training data rather than learning a generalisable mapping. When evaluated on unseen test samples, this overfitting manifests as increased localisation errors. This tendency is exacerbated for larger plate sizes, where the longer signal length produces a higher-dimensional input space. On the 250 mm plate using the 16-sensor configuration, for example, the model is trained on 31,056 input features but only 1020 training samples, which is a severe imbalance that promotes overfitting despite the regularisation employed by ridge regression. The risk is expected to be even greater for the 500 mm plate, where only half as many training samples were available. The elevated MSE values are further amplified by a small number of large prediction errors; because MSE penalises errors quadratically, even a few poorly localised delaminations can substantially inflate the reported performance.

Improved regularisation could potentially mitigate this behaviour, but as with the detection experiments, no hyperparameter tuning was performed for ridge regression in this study. The regularisation parameter was fixed at $\alpha = 1$ for all experiments, and validation-based selection of α may improve robustness. The present results therefore provide strong evidence that the CNN is better suited for delamination localisation, but do not establish a performance ceiling for ridge regression under optimal hyperparameter settings.

Figure 4.12 provides insight into the conditions under which the CNN achieves reliable localisation performance. For all investigated plate sizes, low MSE values are obtained at SNR levels of 20 dB and above, indicating that the model can accurately predict delamination positions under low-noise conditions. The mean MSE values at an SNR of 20 dB are 0.00191, 0.00232, and 0.01068, corresponding to mean RMSE values, in physical units, of 4.37 mm, 12.04 mm, and 51.67 mm for the 100 mm, 250 mm, and 500 mm plates, respectively. From an SHM perspective, these results indicate that the model would substantially reduce the inspection area for the two smaller plates, whereas a considerably larger region would still need to be inspected for the 500 mm plate.

Localisation error increases rapidly below 10 dB. A particularly pronounced reduction in MSE is observed between 10 dB and 20 dB for the 500 mm plate, indicating a stronger dependence on noise level compared with the smaller plates. One possible explanation is that the larger plate results in longer wave propagation distances between the delamination and the sensors. As propagation distance increases, attenuation and dispersion effects become more pronounced, causing wave packets to spread out and their amplitudes to decrease. Damage-related features therefore become less distinct and more susceptible to masking by noise, making localisation more challenging at a given noise level.

At lower noise levels (SNR of 20 dB and above), the 100 mm and 250 mm plates exhibit very similar relative localisation performance, while the 500 mm plate consistently produces higher errors. Several factors likely contribute to this gap, and they are not mutually exclusive. The reduced number of training samples for the 500 mm plate is a natural first candidate, and the data scaling experiments support this interpretation: localisation error decreases monotonically with dataset size for all plate sizes, with the most substantial improvements occurring at smaller dataset sizes. The rate of improvement gradually decreases, with diminishing returns becoming apparent beyond approximately 510 delamination samples. Beyond this point, the network appears to have captured the dominant signal features, and additional data primarily refines rather than substantially improves the learned representation. This suggests that for the smaller plates, further performance gains would require architectural changes rather than simply more data.

However, the data scaling trends are broadly similar across all three plate sizes, implying that a meaningful performance gap for the 500 mm plate would persist even if the number of training samples were equalised. A further contributing factor may therefore be the increased physical spacing between sensors on the larger plates. Although identical sensor configurations were used for all plate sizes, the distance between sensors scales with plate size, and results presented in Figure 4.13 indicate that larger sensor spacing is associated with higher localisation error. This effect may also account for the comparatively small performance difference between the 100 mm and 250 mm plates. Taken together, the reduced dataset size, longer propagation distances, and increased sensor spacing plausibly explain the elevated localisation error for the 500 mm plate, though a systematic investigation isolating each factor individually would be required to quantify their relative contributions.

6
Conclusion

This thesis investigated the use of finite element simulations and machine learning for delamination detection and localisation in composite plates using Lamb wave-based structural health monitoring. By combining numerical simulation with data-driven analysis, a complete methodology was developed for generating labelled datasets and training machine learning models for automated damage assessment.

The first research question concerned how finite element simulations of Lamb wave propagation can be used to generate datasets suitable for machine learning applications. The results demonstrate that explicit finite element simulations provide an efficient means of generating large quantities of labelled guided-wave data while maintaining physically reasonable wave propagation behaviour. The adopted modelling strategy, based on layered shell elements and prescribed displacement excitation, enabled the simulation of 1875 unique delamination scenarios across three plate sizes. Wave field visualisations and attenuation studies confirmed that the simulated wave propagation exhibited expected physical characteristics, including scattering at delaminations and geometric attenuation proportional to $1/\sqrt{r}$. Although several modelling simplifications were introduced to reduce computational cost, the simulations successfully generated datasets containing damage-sensitive signal variations suitable for machine learning.

The second research question addressed how machine learning models can be trained to detect and localise delamination in composite structures using guided wave data. The results demonstrate that supervised learning can be employed by training models on labelled guided wave signals obtained from numerical simulations. In this work, a two-stage framework based on one-dimensional convolutional neural networks was developed, where a classification model first determines the presence of a delamination and a subsequent regression model predicts its location. By learning directly from the temporal sensor signals, the models were able to extract damage-related features without manual feature engineering. The results show that this approach can successfully detect and localise delamination under a range of noise levels and training dataset sizes.

The third research question examined how a convolutional neural network compares with benchmark models under different conditions. For delamination detection, the CNN achieved higher classification accuracy than logistic regression under most investigated noise conditions. However, the CNN also displayed training instability in certain cases, particularly for the largest plate size and under challenging noise conditions, where some training runs failed to converge to meaningful solutions. At an SNR of 20 dB, the CNN achieved classification accuracies of (96.4% ± 7.0%), (99.4% ± 0.5%), and (78.0% ± 23.0%) on the 100 mm, 250 mm, and 500 mm plates, respectively. The accuracy on the 500 mm plate is somewhat misleading, however, as the underlying distribution is bimodal: a subset of runs converged successfully and achieved high classification accuracy, while the remainder failed to converge and plateaued near 50%. For the localisation task, the CNN produced substantially lower prediction errors than ridge regression and exhibited greater robustness to varying dataset sizes and noise levels. With an SNR of 20 dB the CNN achieved MSE values of (0.00191 ± 0.00092), (0.00232 ± 0.00043), and (0.01068 ± 0.00240) on the 100 mm, 250 mm, and 500 mm plate, respectively.

In conclusion, the results show that finite element-generated Lamb wave datasets can be effectively combined with convolutional neural networks to perform automated delamination detection and localisation in composite structures. The proposed methodology provides a scalable framework for developing data-driven structural health monitoring systems while reducing the reliance on costly experimental datasets.

6.1 Future work

An important area for future research is the experimental validation of the finite element methodology. Although the simulated wave propagation exhibited physically reasonable behaviour, agreement with theoretical attenuation characteristics alone is insufficient to verify that the model accurately represents real structures. Experimental measurements on composite specimens would therefore provide valuable validation of the modelling assumptions and improve confidence in the generated datasets. Such experiments would also enable an assessment of how well machine learning models trained on simulated data generalise to measured signals.

Another natural extension is the application of the methodology to more realistic geometries. The present work considered only flat composite plates, whereas practical aerospace structures often contain geometric discontinuities such as curvatures, bolt holes, and thickness transitions. These features influence wave propagation and might be common locations for damage initiation. Investigating more representative geometries would therefore increase the practical relevance of the methodology.

Future studies could furthermore investigate a wider range of damage scenarios and operating conditions. Real structures may contain delaminations of different sizes and shapes, as well as other damage types such as matrix cracking and fibre breakage. Environmental factors, including temperature variations and operational loading, may also affect wave propagation and influence the performance of machine learning models. Incorporating such variations would improve the robustness of the proposed approach.

Finally, alternative machine learning architectures could be explored. In particular, two-dimensional convolutional neural networks operating on time-frequency representations, such as spectrograms, may provide additional information compared to the one-dimensional time-domain approach used in this work. Alternatively, unsupervised anomaly detection methods may represent a promising direction for practical SHM applications. Rather than relying on labelled examples of damage, the model could be trained using measurements collected during normal operation to establish a baseline representation of the healthy structure. Deviations from this baseline could then be identified as potential damage. Such an approach would allow the model to continuously incorporate new data throughout the service life of the structure, potentially improving robustness to structural variations and reducing the dependence on large, labelled datasets.

Bibliography

[1] Y. J. Cha, R. Ali, J. Lewis, and O. Büyükztürk, "Deep learning-based structural health monitoring," *Automation in Construction*, vol. 161, May 2024. DOI: 10.1016/J.AUTCON.2024.105328.

[2] Z. Su, L. Ye, and Y. Lu, "Guided lamb waves for identification of damage in composite structures: A review," *Journal of Sound and Vibration*, vol. 295, pp. 753–780, Aug. 2006. DOI: 10.1016/J.JSV.2006.01.020.

[3] M. Rautela and S. Gopalakrishnan, "Ultrasonic guided wave based structural damage detection and localization using model assisted convolutional and recurrent neural networks," *Expert Systems with Applications*, vol. 167, Apr. 2021. DOI: 10.1016/j.eswa.2020.114189.

[4] V. Ewald, R. S. Venkat, A. Asokkumar, R. Benedictus, C. Boller, and R. M. Groves, "Perception modelling by invariant representation of deep learning for automated structural diagnostic in aircraft maintenance: A study case using deepshm," *Mechanical Systems and Signal Processing*, vol. 165, Feb. 2022. DOI: 10.1016/J.YMSSP.2021.108153.

[5] Z. Yang et al., "A review on guided-ultrasonic-wave-based structural health monitoring: From fundamental theory to machine learning techniques," *Ultrasonics*, vol. 133, Aug. 2023. DOI: 10.1016/J.ULTRAS.2023.107014.

[6] M. Lundgren and G. Lindström, "Numerical simulation of lamb wave propagation for detection of damage in composite structures," M.S. thesis, Linköping University, 2025.

[7] B. D. Agarwal, L. J. Broutman, and K. Chandrashekhara, *Analysis and Performance of Fiber Composites*, Third Edition. John Wiley & Sons, Inc., 2006.

[8] V. Giurgiutiu, *Structural Health Monitoring with Piezoelectric Wafer Active Sensors*, Second Edition. Academic Press, 2014, pp. 293–355. DOI: https://doi.org/10.1016/B978-0-12-418691-0.00006-X.

[9] C. Willberg, S. Eisenträger, J. Perez, D. Schmicker, and U. Gabbert, "Comparison of different higher order finite element schemes for the simulation of lamb waves," *Computer Methods in Applied Mechanics and Engineering*, vol. 241-244, pp. 246–261, Oct. 2012. DOI: 10.1016/j.cma.2012.06.011.

[10] Z. Su and L. Ye, "Identification of damage using lamb waves: From fundamentals to applications," *Lecture Notes in Applied and Computational Mechanics*, vol. 48, 2009. DOI: 10.1007/978-1-84882-784-4.

[11] S. Anton, "Baseline-free and self-powered structural health monitoring," Jul. 2008.

[12] J. L. Rose, *Ultrasonic guided waves in solid media.* Cambridge University Press, 2014. DOI: 10.1017/CBO9781107273610.

[13] B. Chen, Y. Zhang, Q. Wang, H. Zhang, and Y. Wang, "The signal analysis of lamb wave in steel plates strengthened by cfrp with interface debonding," *Ocean Engineering*, vol. 283, 2023. DOI: 10.1016/j.oceaneng.2023.115061.

[14] J. Plesek, R. Kolman, and D. Gabriel, "Estimation of critical time step for explicit integration," *18th International Conference on Engineering Mechanics*, 2012.

[15] J. Hallquist, *LS-DYNA® theory manual.* 2006.

[16] K. P. Murphy, *Probabilistic Machine Learning: An introduction.* MIT Press, 2022. [Online]. Available: http://probml.github.io/book1.

[17] B. Mehlig, *Machine Learning with Neural Networks: An Introduction for Scientists and Engineers.* Cambridge University Press, 2022, pp. 141–154.

[18] A. E. Hoerl and R. W. Kennard, "Ridge regression: Biased estimation for nonorthogonal problems," *Technometrics*, vol. 12, 1 1970. DOI: 10.2307/1267351.

[19] K. P. Murphy, *Machine learning: a probabilistic perspective.* The MIT Press, 2012, pp. 245–252.

[20] A. Huber, "The dispersion calculator - a free software for calculating dispersion curves of guided waves," *e-Journal of Nondestructive Testing*, vol. 29, 6 2024. DOI: 10.58286/29894.

[21] K. J. Bathe, *Finite Element Procedures*, Second Edition. 1996.

[22] F. Moser, L. J. Jacobs, and J. Qu, "Modeling elastic wave propagation in waveguides with the finite element method," *NDT and E International*, vol. 32, 4 1999. DOI: 10.1016/S0963-8695(98)00045-0.

[23] C. Willberg, S. Duczek, J. M. Vivar-Perez, and Z. A. Ahmad, "Simulation methods for guided wave-based structural health monitoring: A review," *Applied Mechanics Reviews*, vol. 67, Jan. 2015. DOI: 10.1115/1.4029539.

[24] G. E. Hinton, N. Srivastava, A. Krizhevsky, I. Sutskever, and R. R. Salakhutdinov, "Improving neural networks by preventing co-adaptation of feature detectors," Jul. 2012. [Online]. Available: https://arxiv.org/pdf/1207.0580.

A

Complementary results

This chapter contains complementary results not presented in the results section. This includes results obtained from the tests conducted on the 100 mm and 500 mm plates, as well as complementary results using the 8-sensor configuration.

A.1 Delamination detection

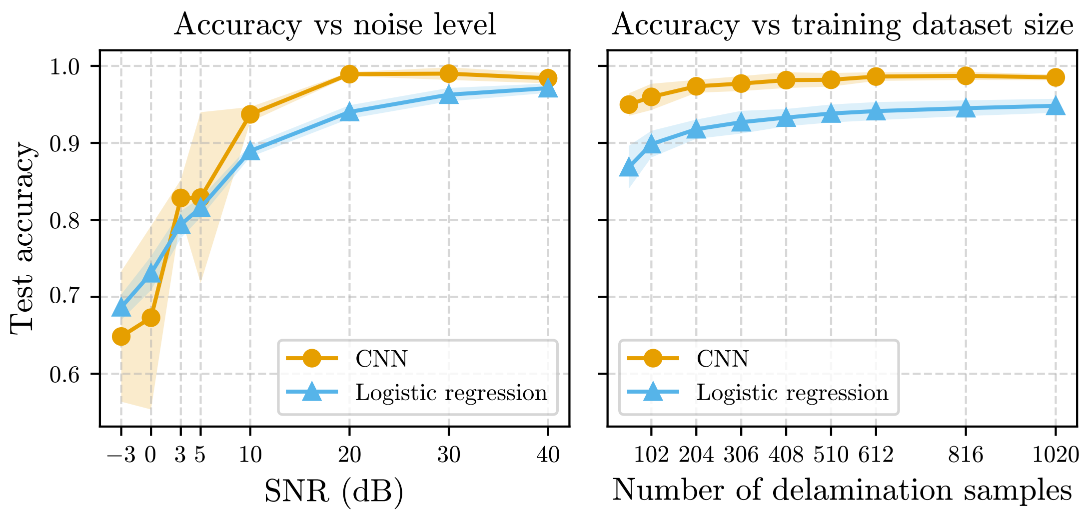

Figure A.1: Comparison of delamination detection accuracy for the CNN and logistic regression models on the 100 mm plate using 8 sensors. Solid lines represent the mean accuracy across ten runs, while shaded regions indicate ±1 standard deviation.

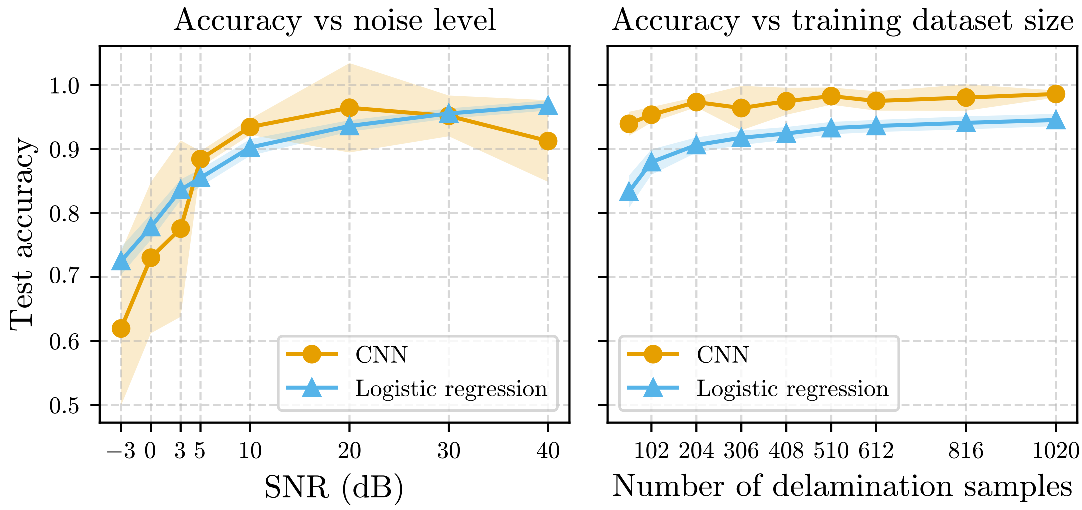

Figure A.2: Comparison of delamination detection accuracy for the CNN and logistic regression models on the 100 mm plate using 16 sensors. Solid lines represent the mean accuracy across ten runs, while shaded regions indicate ±1 standard deviation.

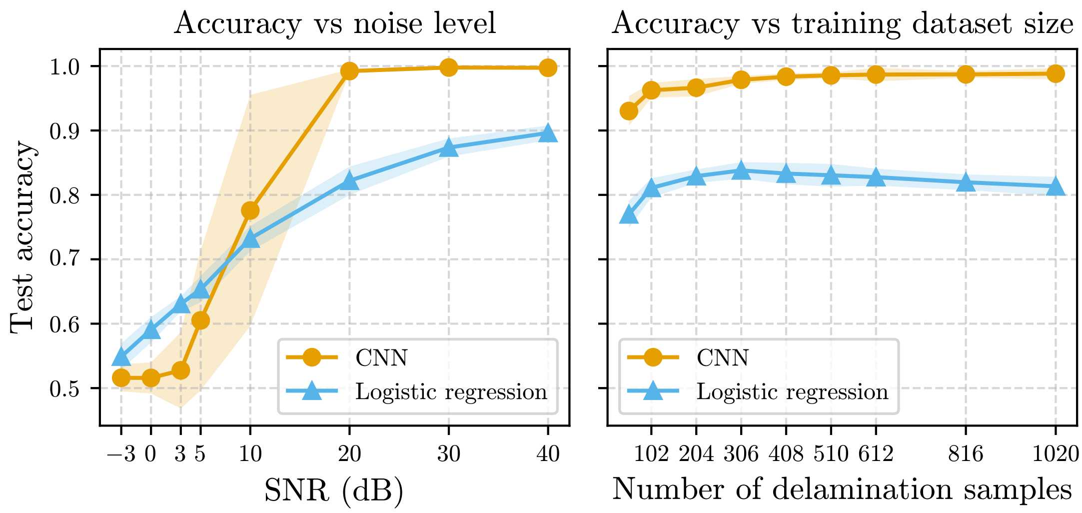

Figure A.3: Comparison of delamination detection accuracy for the CNN and logistic regression models on the 250 mm plate using 8 sensors. Solid lines represent the mean accuracy across ten runs, while shaded regions indicate ±1 standard deviation.

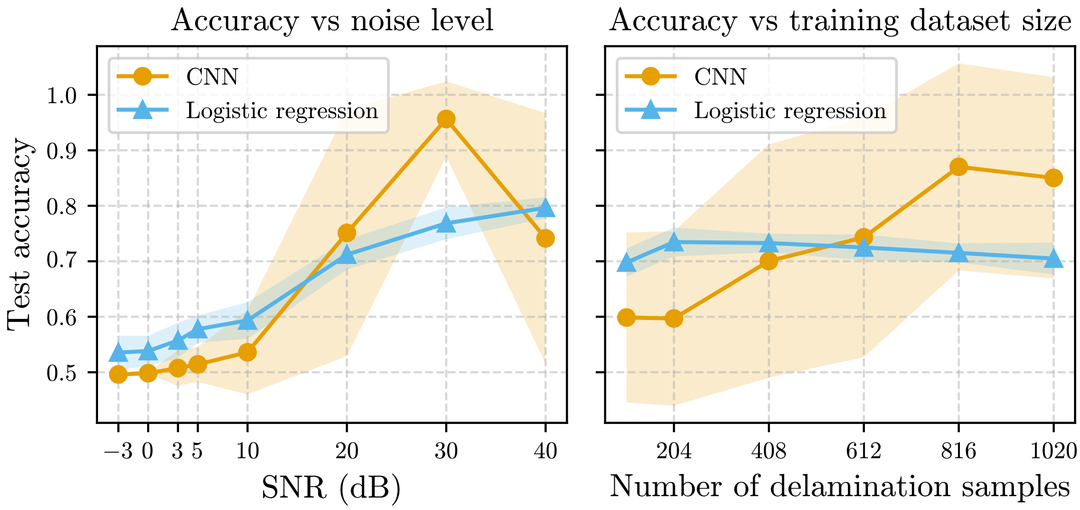

Figure A.4: Comparison of delamination detection accuracy for the CNN and logistic regression models on the 500 mm plate using 8 sensors. Solid lines represent the mean accuracy across ten runs, while shaded regions indicate ±1 standard deviation.

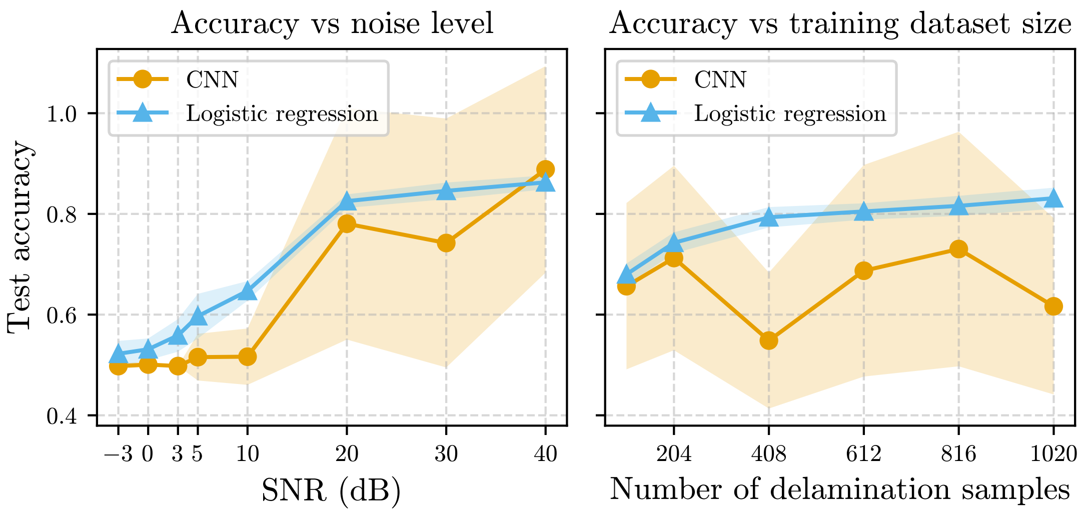

Figure A.5: Comparison of delamination detection accuracy for the CNN and logistic regression models on the 500 mm plate using 16 sensors. Solid lines represent the mean accuracy across ten runs, while shaded regions indicate ±1 standard deviation.

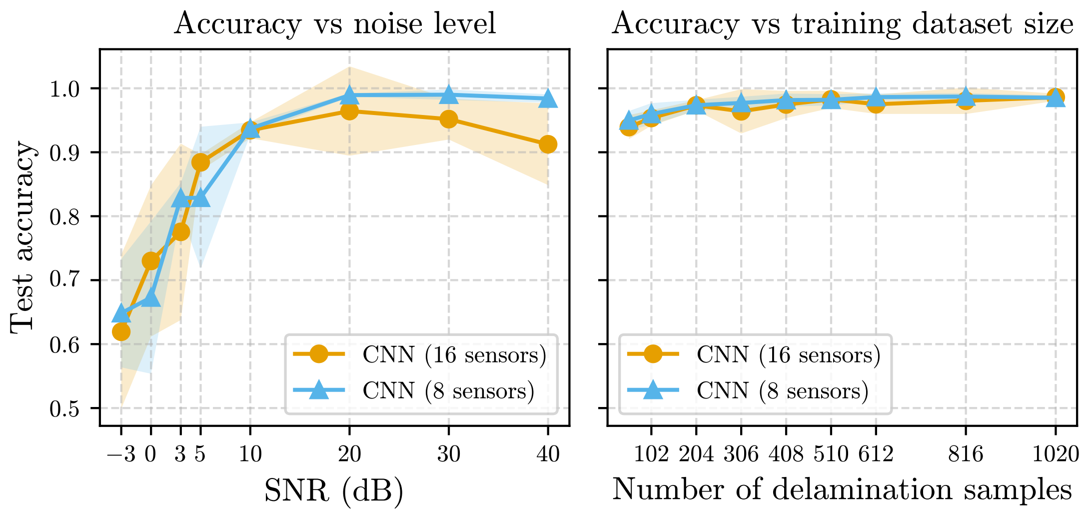

Figure A.6: Comparison of delamination detection accuracy for the CNN model on the 100 mm plate using 8, and 16 sensors, respectively. Solid lines represent the mean accuracy across ten runs, while shaded regions indicate ±1 standard deviation.

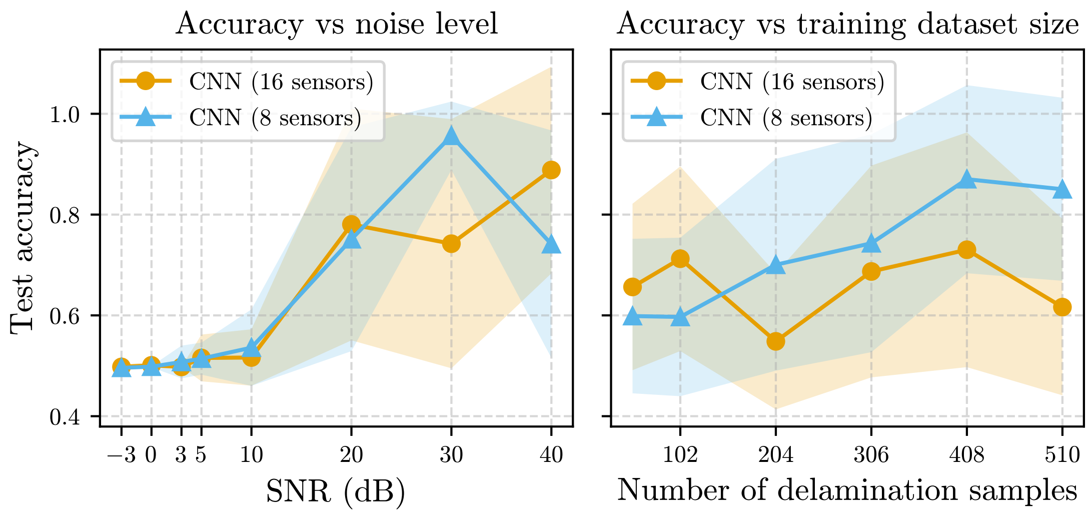

Figure A.7: Comparison of delamination detection accuracy for the CNN model on the 500 mm plate using 8, and 16 sensors, respectively. Solid lines represent the mean accuracy across ten runs, while shaded regions indicate ±1 standard deviation.

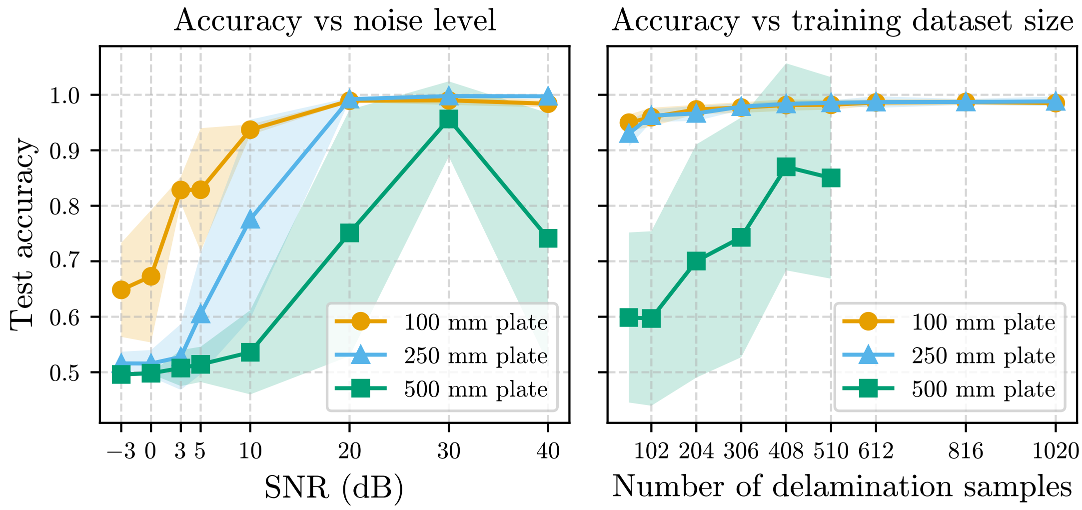

Figure A.8: Comparison of delamination detection accuracy for the CNN model on three different plate sizes using 8 sensors. Solid lines represent the mean accuracy across ten runs, while shaded regions indicate ±1 standard deviation.

A.2 Delamination localisation

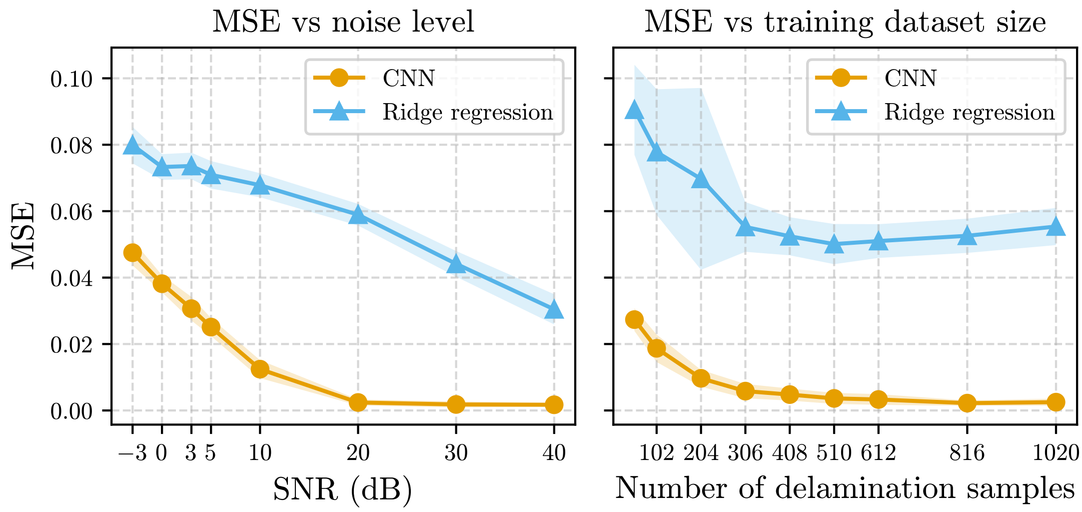

Figure A.9: Comparison of delamination localisation MSE for the CNN and ridge regression models on the 100 mm plate using 8 sensors. Solid lines represent the mean MSE across ten runs, while shaded regions indicate ±1 standard deviation.

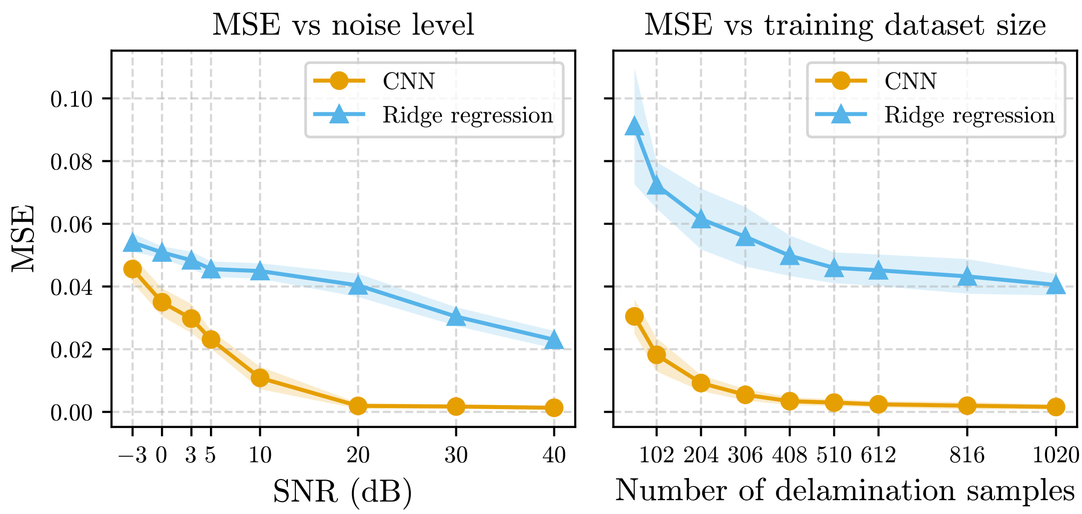

Figure A.10: Comparison of delamination localisation MSE for the CNN and ridge regression models on the 100 mm plate using 16 sensors. Solid lines represent the mean MSE across ten runs, while shaded regions indicate ±1 standard deviation.

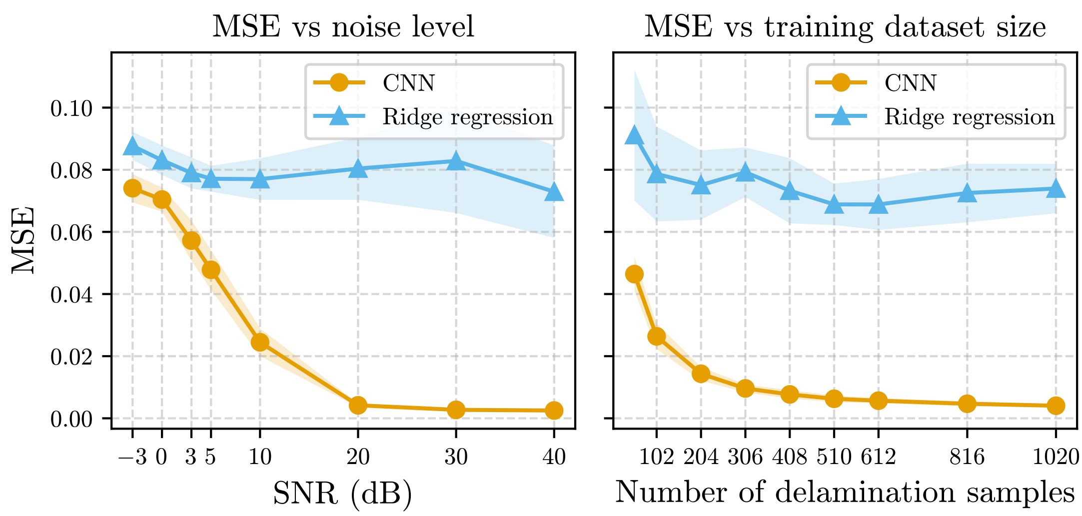

Figure A.11: Comparison of delamination localisation MSE for the CNN and ridge regression models on the 250 mm plate using 8 sensors. Solid lines represent the mean MSE across ten runs, while shaded regions indicate ±1 standard deviation.

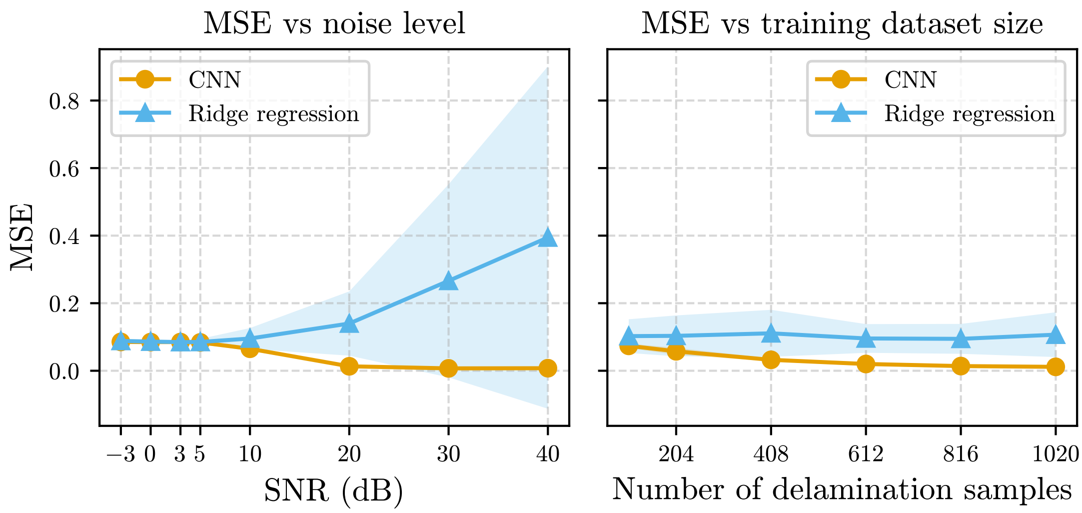

Figure A.12: Comparison of delamination localisation MSE for the CNN and ridge regression models on the 500 mm plate using 8 sensors. Solid lines represent the mean MSE across ten runs, while shaded regions indicate ±1 standard deviation.

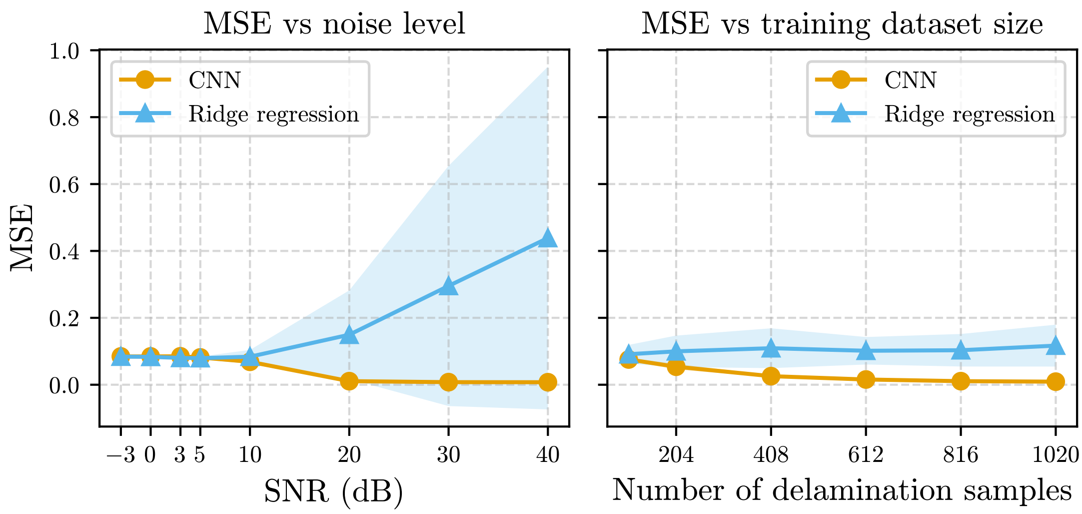

Figure A.13: Comparison of delamination localisation MSE for the CNN and ridge regression models on the 500 mm plate using 16 sensors. Solid lines represent the mean MSE across ten runs, while shaded regions indicate ±1 standard deviation.

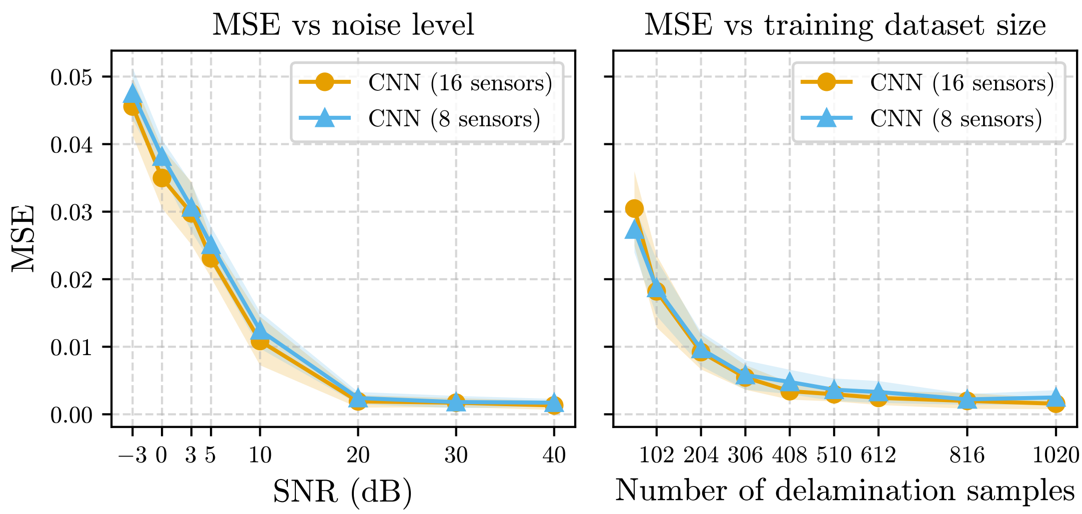

Figure A.14: Comparison of delamination localisation MSE for the CNN model on the 100 mm plate using 8, and 16 sensors, respectively. Solid lines represent the mean MSE across ten runs, while shaded regions indicate ±1 standard deviation.

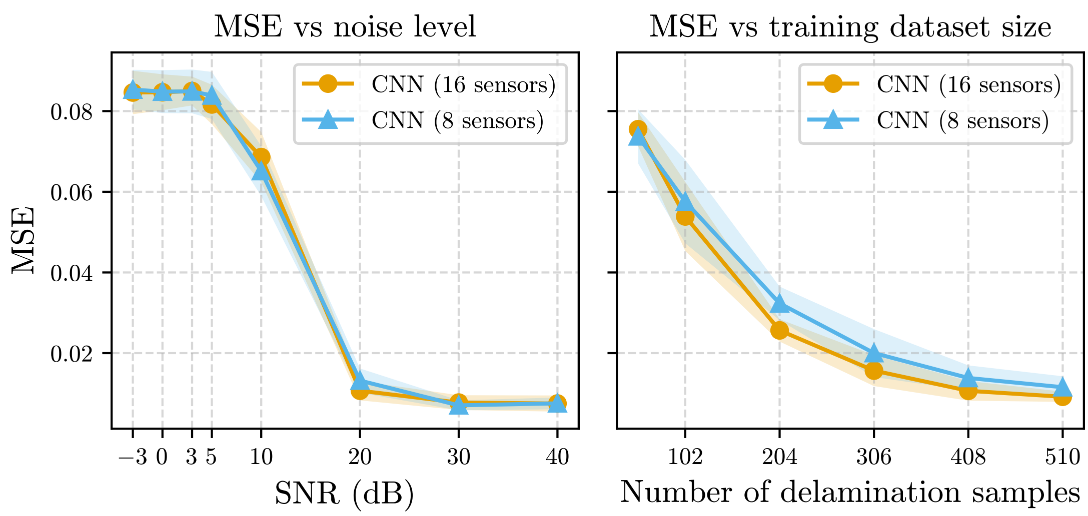

Figure A.15: Comparison of delamination localisation MSE for the CNN model on the 500 mm plate using 8, and 16 sensors, respectively. Solid lines represent the mean MSE across ten runs, while shaded regions indicate ±1 standard deviation. Greater robustness at intermediate noise levels for the 16-sensor configuration.

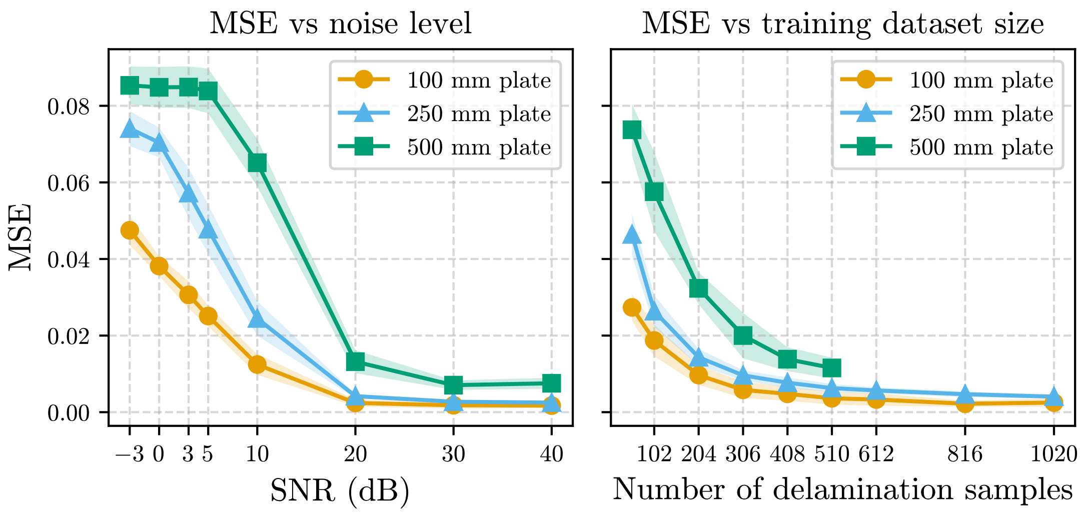

Figure A.16: Comparison of delamination localisation MSE for the CNN model on three different plate sizes using 8 sensors. Solid lines represent the mean MSE across ten runs, while shaded regions indicate ±1 standard deviation.

DEPARTMENT OF INDUSTRIAL AND MATERIALS SCIENCE
CHALMERS UNIVERSITY OF TECHNOLOGY
Gothenburg, Sweden
www.chalmers.se

AVANCEZ
1829

CHALMERS
UNIVERSITY OF TECHNOLOGY